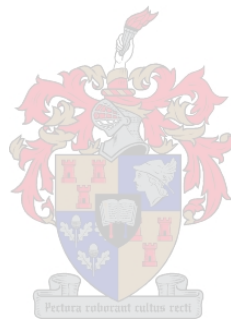


Hip position tracking device

by
Philippus Johannes van Niekerk

*Thesis presented in partial fulfilment of the requirements for the degree
of Master of Engineering (Mechanical) in the Faculty of Engineering at
Stellenbosch University*



Supervisor: Dr Jacobus Hendrik Müller

April 2019

Declaration

By submitting this thesis electronically, I declare that the entirety of the work contained therein is my own, original work, that I am the sole author thereof (save to the extent explicitly otherwise stated), that reproduction and publication thereof by Stellenbosch University will not infringe any third party rights and that I have not previously in its entirety or in part submitted it for obtaining any qualification.

Date: April 2019

Copyright © 2019 Stellenbosch University
All rights reserved

Abstract

Hip position tracking device

P.J. van Niekerk

Department of Mechanical and Mechatronic Engineering

Stellenbosch University

Thesis: MEng (Mech)

April 2019

A robust, user-friendly hip position tracking device that is capable to function outside of a lab environment can lead to valuable progression in the hip impingement research field. This project discusses the design and testing of such a device.

The device developed functions by tracking a permanent magnet on the thigh with magnetometers placed on the pelvis to classify the relative angle between the pelvis and the femur (hip angle). The position tracking device only tracks if the user reaches a specific hip angle that is of interest. The angle is set by the user in the calibration procedure. The device classifies the position of interest, as indicated by the user, with a k-nearest neighbours (k-NN) algorithm.

The device was verified for accuracy against a Vicon Vantage motion capture system. Five participants took part in the study structured in a two-tier structure. The first tier was to evaluate the method of motion capture. The second tier's objective was to verify the accuracy of the device.

The algorithm output is the amount of calibrated "nearest neighbours" expressed as a percentage activated at the current pose. For a 100 % output, the device is accurate below 5 ° in all three anatomical angles of the hip.

Uittreksel

Heup posisie toestel

P.J. van Niekerk

Departement Meganiese en Megatroniese Ingenieurswese

Universiteit Stellenbosch

Tesis: MIng (Mech)

April 2019

'n Robuuste, gebruikersvriendelike heup posisie metingstoestel wat buite 'n laboratorium gebruik kan word sal 'n geweldige bydrae lewer tot die heup *impingement* navorsingsveld. Hierdie projek bespreek die ontwerp en toets van 'n toestel.

Die toestel is geverifieer vir akkuraatheid teen 'n *Vicon Vantage* bewegingsopvangstelsel. Vyf deelnemers het deelgeneem aan die studie wat gestruktureer was in twee vlakke. Die eerste vlak was om die metode van bewegingsopname te evalueer. Die tweede vlak was om die akkuraatheid van die toestel te verifieer.

Die toestel wat ontwikkel is funksioneer deur die magneetveld om 'n permanente magnet te meet. Die magneet word geplaas op die femur en die magnetiesesensore op die bekkenbeen. Die relatiewe hoek tussen die bekkenbeen en die femur (heuphoek) kan so bereken word en geklassifiseer word. Die toestel meet slegs as die gebruiker 'n spesifieke heuphoek wat van belang is bereik. Die hoek word deur die gebruiker in die kalibrasieprosedure gestel. Die toestel klassifiseer die posisie van belang, soos aangedui deur die gebruiker, met 'n k-naaste bure (k-NN) algoritme.

Die algoritme-uitset is die hoeveelheid gekalibreerde "naaste bure", uitgedruk as 'n persentasie. Vir 'n 100 % uitset is die toestel akkuraat onder 5° in al drie anatomiese hoeke van die heup.

3.4.1	Microcontroller code	36
3.4.2	Sensor libraries	39
3.4.3	GUI and data-capturing	39
3.4.4	Python post-processing code	41
3.5	Machine learning.....	42
3.5.1	Algorithm selection	42
3.5.2	Model implementation	43
3.6	System synthesis	46
3.6.1	Hardware placement.....	46
3.6.2	Magnet selection	47
4	Pilot study	49
4.1	Participant inclusion/exclusion criteria:	49
4.2	Pilot study 1	49
4.2.1	Protocol	49
4.2.2	Results: Pilot study 1	51
4.2.3	Discussion: Pilot study 1	55
4.3	Pilot study 2	56
4.3.1	Protocol	56
4.3.2	Objectives	56
4.3.3	Results: Pilot study 2	56
4.3.4	Discussion: Pilot study 2	62
5	Conclusion.....	65
5.1	Device design	65
5.2	Outcomes.....	65
5.3	Future work.....	66
6	References	67
	Appendix A: Ethical approval.....	72
	Appendix B: Results	74
	Appendix C: Normal hip range of motion.....	78
	Appendix D: Review of studies	79

List of figures

Figure 1: Graphical representation of pincer (left) and cam (right) impingement (Volpon, 2016).	2
Figure 2: Scaling error.....	11
Figure 3: Misalignment error	12
Figure 4: Bias error	12
Figure 5: Actual and target magnetic flux density	14
Figure 6: Multiple actual and target magnetic flux densities	15
Figure 7: Instance-based learning (Géron, 2017)	19
Figure 8: Model-based learning (Géron, 2017).....	20
Figure 9: Validation curve (Géron, 2017)	21
Figure 10: Learning curve (Pedregosa <i>et al.</i> , 2011)	22
Figure 11: The femoral and pelvic coordinate system (“ISB recommendation on definitions of joint coordinate system”, 2002).....	25
Figure 12: Systems engineering approach	26
Figure 13: Conceptual design.....	26
Figure 14: Preliminary design process.....	31
Figure 15: Device function	32
Figure 16: RM3100 magnetometer (PNI Corporation, 2016).....	34
Figure 17: Magnet layout (not to scale)	35
Figure 18: Software interactions.....	36
Figure 19: Microcontroller code flow diagram	38
Figure 20: GUI tabs from left to right, top to bottom. Connect, training, test training and reading tabs	40
Figure 21: Kivy logic.....	41
Figure 22: Post-processing data flow	42
Figure 23: Hardware placement	47
Figure 24: Pilot study 1 machine learning pipeline.....	52
Figure 25: Difference in angle (error) calculation for pilot study 1	53
Figure 26: Average error and standard deviation in flexion/extension.....	54
Figure 27: Average error and standard deviation in ab/adduction	54

Figure 28: Average error and standad deviation in internal/ external rotation .. 55

Figure 29: Difference in angle calculation for pilot study 2 58

Figure 30: Absolute difference in the angle between the average point of interest for the percentage nearest neighbours closest to the point of interest for different values of I in flexion / extension 59

Figure 31: Absolute difference in the angle between the average point of interest for the percentage nearest neighbours closest to the point of interest for different values of I in the abduction/adduction 59

Figure 32: Absolute difference in the angle between the average point of interest for the percentage nearest neighbours closest to the point of interest for different values of I in the internal/external rotation 60

Figure 33: Calculating the false negatives flow diagram..... 61

Figure 34: False negative instances for k in k-nn for different tolerance zones .. 62

Figure 35: Percentage nearest neighbours closest to the point of interest and hip angle for 5 squats..... 74

Figure 36: Percentage nearest neighbours closest to the point of interest and hip angle for 5 squats..... 75

Figure 37: Hip angle data from Vicon for squat movement..... 76

Figure 38: Hip angle data from Vicon for lunge movement..... 77

Figure 39: Hip angle data from Vicon for squat movement..... 77

List of tables

Table 1: Confusion matrix.....	23
Table 2: Feasibility study	30
Table 3: System allocation	33
Table 4: Regression model parameters.....	44
Table 5: Classification model parameters	45
Table 6: Movement tasks	50
Table 7: False positive section of the confusion matrix	57
Table 8: Confusion matrix being addressed in the following section	60

Nomenclature

ASIS	Anterior superior iliac spine
CDC	Central Disciplinary Committee
CT	Computed tomography
GUI	Graphical user interface
IDE	Interactive development environment
IMU	Inertial measurement units
KNN	K-nearest neighbours
ROM	Range of motion
SCL	Serial clock line
SMOTE	Synthetic Minority Oversampling Technique
SVD	Single value decomposition

Symbols

A	Magnetic field error matrix
a	Magnetic field error scalar
B	Magnetic flux density vector
b	Bias error vector
b_e	Bias error vector due to external magnetic “sources”
B_{earth}	Magnetic flux density vector of the earth
B_r	Residual magnetic flux density
B_x	Magnetic flux density (x-direction)
B_y	Magnetic flux density (y-direction)
B_z	Magnetic flux density (z-direction)
c	Speed of light in a vacuum
D	Design matrix
l	Ellipsoid constraint equation parameter
J	Ellipsoid constraint equation parameter
j	Current density
k	Constant in the ellipsoid constraint equation
M	Misalignment error vector
m	Magnetic dipole moment vector
N	Inverse of misalignment error vector
n_x	Misalignment error (x-direction)
n_y	Misalignment error (y-direction)
n_z	Misalignment error (z-direction)
r	Radius vector
S	Scale error matrix
S_x	Scale error (x-direction)
S_y	Scale error (y-direction)
S_z	Scale error (z-direction)
v	Constants vector for the general ellipsoid equations

\mathbf{X}_i	General equation for an ellipsoid dataset vector
ϵ_0	Permittivity of free space
μ_0	Permeability of free space constant
λ	LaGrange multiplier

1 Introduction

Femoroacetabular impingement (FAI) or hip impingement is the abnormal contact of the proximal femur with the acetabulum (Packer and Safran, 2015). Currently, only symptoms, clinical signs and imaging findings are taken into account when diagnosing this motion-related disorder (Griffin *et al.*, 2016). This project aims to develop a specific motion position tracking device for the hip to help answer orthopedic questions in the field of hip impingement.

1.1 Background

Hip impingement morphology is a critical aspect of diagnosing hip impingement. In simple terms, hip impingement morphology refers to the shape of the hip's bone structure that is associated with hip impingement. The method of how these shapes are defined is discussed later in this section.

Some studies suggest that the incidence of hip impingement morphology in the general population is as much as 67 % (Frank *et al.*, 2015). Having hip impingement morphology does not always lead to symptoms associated with hip impingement. The symptoms include pain and stiffness in and around the hip joint (Volpon, 2016). There is a gap in the literature to explain the link between symptomatic and asymptomatic hip impingement. Asymptomatic hip impingement is when a patient has hip impingement morphology but no symptoms. Symptomatic hip impingement is when a patient has hip impingement morphology and symptoms associated with hip impingement.

An international, multidisciplinary consensus was set up after experts in the field recognized that there is a difference in opinion regarding the definition and treatment of hip impingement (Griffin *et al.*, 2016). A consensus of what hip impingement is and a clarification of the terminology used in the field was reached. A new term, FAI or hip impingement syndrome was coined to distinguish the clinical disorder. The consensus reached for the definition of hip impingement syndrome was:

FAI syndrome – “FAI syndrome is a motion-related clinical disorder of the hip with a triad of symptoms, clinical signs and imaging findings. It represents symptomatic premature contact between the proximal femur and the acetabulum.”



Figure 1: Graphical representation of pincer (left) and cam (right) impingement (Volpon, 2016).

As it is indicated above, hip impingement morphology is only one part of hip impingement syndrome. The other two being symptoms and clinical signs. Hip impingement morphology can be categorized as follows: Cam impingement, pincer impingement or both (Packer and Safran, 2015). Cam impingement is characterized by an aspherical femoral head (ball in the ball-and-socket joint of the hip). Pincer impingement can be described as acetabular overcoverage of the femoral head. This can be caused by a too deep acetabulum socket or misalignment of the acetabulum to the femoral head (Volpon, 2016).

An X-ray is sufficient to diagnose FAI morphology, but a computed tomography (CT) or MRI can also be used (Griffin *et al.*, 2016). Cam impingement is diagnosed by measuring the alpha angle of the femoral head. The alpha angle is the angle between the femoral head axis and the point where the femoral head begins to form aspherical. The origin of the angle is in the center of the femoral head (Paul and Frederick, 2005; Siebenrock *et al.*, 2009). It is difficult to define “normal” cam morphology with the alpha angle but angles below 42 ° is generally accepted (Volpon, 2016).

Pincer impingement is more difficult to define. Due to the complex nature of this impingement, a better way to define both cam and pincer impingement is through an impact study. It refers to a 3D simulation in which a CT scan is used to establish impingement points in the hip joint (Röling *et al.*, 2015). The simulation determines where a patient’s hip will impinge when taken through the normal range of motion. The normal range of motion in this instance is defined in Appendix C.

Although surgery is a proven treatment to relieve the symptoms of symptomatic FAI, it is unclear whether surgery is necessary for asymptomatic FAI (Bedi *et al.*, 2008; Ng *et al.*, 2010; Fairley *et al.*, 2016). Three major considerations are that the occurrence of joint damage in asymptomatic hip impingement is not proven yet. Secondly, there is no evidence to support the fact that surgery will prevent joint damage (Griffin *et al.*, 2016). And thirdly, FAI is more prevalent in young active individuals (Frank *et al.*, 2015). However, although there is a lack of sufficient evidence to support the progression of osteoarthritis (OA) in asymptomatic FAI, there is some indication that a large alpha angle can be associated with OA (Parvizi, Leunig and Ganz, 2007; Agricola *et al.*, 2013).

Despite the correlations and several studies suggesting FAI may cause OA, sufficient evidence does not yet exist to prove the fact. (Ng *et al.*, 2010; Fairley *et al.*, 2016). The need for further study is even greater following these considerations because surgeons do not want to operate if patients are asymptomatic, especially if the patient is still a child and not fully grown. On the other hand, if the risk of developing OA could be reduced at an early stage it will be better than trying to fix the joint damage after it occurred. It is intuitive to think that joint damage occurs when an individual impinges, though it is not proven yet. Whether joint damage always causes symptoms is unknown.

While the concept of hip impingement from a bone structure point of view may be simple, determining if an individual impinges is a difficult task. Medical imaging is the best solution currently available. The link between impingement morphology and range of motion limitations is not well understood. Soft tissue limitation plays an important role in this relationship. The commercial software tries to predict the range of motion (ROM) limitations due to impingement, but it is not validated (Röling *et al.*, 2015). The device proposed by this project to fill in the gap in hip impingement research is a hip position tracking device. As stated above, only symptoms, clinical signs and imaging are taken into account when diagnosing hip impingement syndrome. A device that takes the kinematics of the hip into account is needed to understand hip impingement better.

The device will aid in answer research questions, like the most important question identified at the Warwick consensus “In those with FAI morphology, can we predict who will become symptomatic?” (Griffin *et al.*, 2016). Research into questions like these is difficult to answer with the motion tracking devices currently available. Commercially available devices are either restricted to the lab or are not robust enough to be used during most sports.

The device developed in this project hip position detection device. The device will only detect if a person reaches a calibrated ROM point. This data, in conjunction with the triad of hip impingement syndrome symptoms can be used to better understand the syndrome

1.2 Aim

The aim of the project is to develop and validate a device able to predict if the hip joint reaches a specific position within 5 ° in all three degrees of freedom of the hip. The accuracy of the device will be validated by comparing the device against a gold standard optical motion tracking system.

1.3 Requirements

A short discussion of the requirements follow. It must be clarified that the motion position tracking device developed does not track if an individual's hip impinges, it only tracks if an individual reaches a position in the range of motion of the hip joint. The aim of the device is to accurately predict if the hip joint reaches a specific position. The aim is better clarified in a set of requirements for the device. The requirements were developed in section 3.1.4 following the analysis of the client's needs.

1. Robust: The device must be robust enough to be used during a variety of sports game including impact sports, for example, rugby. The device must be able to be encapsulated with a protective capsule to shield the device. The final device needs to be protected with the International Protection Marking (IP) 67 class enclosure. The standard is in accordance with the International Electrotechnical Commission (IEC) 60529 standard.
2. Accurate: The device must be accurate over extended periods of time (at least 24 h). An accuracy of 5 ° in all three anatomical angles of the hip joint is necessary to provide sufficient information to the doctor.

The device should be able to be used in a rugby match and be accurate despite the nature of contact sports.

3. User-friendly in use: The device must not impact the player when competing in the sport. In this case, the user refers to the patient. This requirement will be evaluated subjectively.
4. Stand-alone device: The device must be able to operate outside the lab environment.

All the requirements will not be tested in the study. The accuracy requirement will be tested through a pilot study and the user-friendly in use requirement will be evaluated subjectively by the researcher and the pilot study participants. The stand-alone device requirement will be evaluated in the pilot study. The reason for including the requirements that are not thoroughly evaluated is for the

researcher to stay cognizant of the requirement when selecting the appropriate technology.

2 Literature review

The concepts discussed in this chapter is of importance in the device design and evaluation phase of the project.

2.1 Motion tracking

There are two broad categories of motion tracking devices available on the market: Optical and non-optical. Optical systems make use of stationary cameras to track specific markers placed on the object. These systems are regarded as the gold standard for motion tracking. Non-optical systems make use of microelectromechanical systems (MEMS) that consist of inertial measurement units (IMU) and a magnetic sensor. For this project, non-optical sensors will be used to meet the objectives motioned above.

Most MEMS motion tracking devices consist of an accelerometer, gyroscope, and magnetic sensor. The combination of the three sensors will be referred to as IMU sensors although magnetometers are not inertia-based. An accelerometer is a spring-mass system where the mass displaces under acceleration. The displacement of the mass is measured either with a capacitive element or piezo-resistive elements. A Gyroscopes measure angular velocity by vibrating a beam and measuring the Coriolis Effect forces on the beam due to external rotations. This is also done by piezoresistive elements or capacitive elements. Magnetometers measure the magnetic field and are applied in most instances to measure the orientation of the sensor relative to the earth's magnetic field. These sensor units are self-contained which is a significant advantage over optical units because it is not confined to a motion capture lab. The size of the sensor units has limited the application in the past but due to advances in the field, it shrunk down considerably.

A big problem in the industry has been to accurately estimate motion (displacement) from the measured acceleration (accelerometer), angular velocity (gyroscope) and heading (magnetometer). The errors resulting from the estimation is known as drift. Sensor fusion algorithms have tried to combat this by taking the "best" part of each sensor and combining it with a better approximation. The problem is that measurements over a long time period will experience a significant amount of drift, despite implementing sensor fusion (Cockcroft, 2015). To combat the drift in human motion analysis a biomechanical model can be made to add kinetic constraints to the model, but this method adds complexity to the calibration of the sensors and increases the difficulty in setup. The accuracy of an IMU sensor approach in measuring hip angles can be very high. Cockcroft (2015) achieved a mean accuracy of 0.8°, 6.7° and 2.2° in the sagittal, frontal and transverse plane respectively with Xsens (B.V. Technologies, Enschede, Netherlands) MTw development kit. These accuracies were however only

achieved over a short period of time and there were large variabilities. This points to the fact that the IMU's are difficult to set up and achieve accurate results. The Xsens IMU's used by Cockcroft is accepted as an industry leader in IMU based motion tracking and is very expensive (Seel, Raisch and Schauer, 2014). Another study proved that self-developed, cheaper IMU's can produce accurate results. The study by Lin et al. (2011) was not specific to the hip joint but proved cheaper, self-developed IMU sensor can be accurate. Lin et al.'s (2011) sensors produced a root mean square error of 1.75 °, 1.96 ° and 5.46 ° in the three respected degrees of freedom. There are hundreds of IMU based motion tracking studies and depending on the biomechanical model, sensor and calibration procedure used the accuracy results differ greatly. Appendix D reviews the most significant studies related to the project. The researcher decided not to add the studies to the literature review because the IMU-based technology was ultimately not chosen.

The project is going to investigate two technologies to solve the problem at hand. The previously mentioned IMU-based device with inertial and magnetometer sensors will be investigated. Secondly, a more novel approach will be followed, using magnetometers and permanent magnets. Most of the self-developed IMU based systems have the same core hardware layout (Olivares *et al.*, 2011; Hamdi and Awad, 2014; Lambrecht and Kirsch, 2014; Llamas *et al.*, 2017). They consist of an IMU unit on the relevant limbs. The IMU unit houses the accelerometer, magnetometer, and the gyroscope. All these sensors can be mounted to a single chip (Lambrecht and Kirsch, 2014). The sensors are then connected to a microprocessor that processes the data from the sensors and supplies the sensor with power.

While there are a lot of studies using IMU sensors there have however been interesting developments in the field of magnetometers. Several studies proved that one can determine the position a permanent magnet in 3D space near a magnetometer. Determining the position of a magnet over a short distance has been very successful (Schott, Racz and Ag, no date; Chen *et al.*, 2013; Kortier *et al.*, 2015). There are two problems experienced by this approach. Firstly, there is a lot of magnetic field noise near ferromagnetic materials. Secondly, one cannot measure more than one permanent magnet in 3D space at any given moment. The main advantages of this approach are that the system will be more robust and smaller. It would be smaller because instead of placing two inertial and magnetometer units to measure a relative angle, the magnetic tracking approach would only use one sensor and one magnet. This would aid in the robustness of the system. The magnetic system will also not experience the drift related with inertial and magnetometers units because it measures position directly.

2.2 Magnetostatics and magnetometers

In this section magnetic fields, permanent magnets and magnetometers are being discussed as it relates to the device design in section 3. Magnetic fields are discussed in the context permanent magnets.

2.2.1 Magnetostatics

Magnetostatics is the theory of the magnetic fields produced by steady currents (Griffiths, 1999). In this section, Maxwell's equations for magnetostatics are going to be discussed in the context of the project (Feynman, Leighton and Sands, 2010). Deriving equation 2.1 and 2.2 and simplifying these equations are out of the scope of this report. The reason for including them is to gain insight into a magnetic flux density field. \mathbf{B} is the magnetic flux density measured in Tesla [T], c is the speed of light in a vacuum, \mathbf{j} is the current density [A/m²] and ϵ_0 the permittivity of free space.

$$\nabla \cdot \mathbf{B} = 0 \quad (2.1)$$

$$c^2 \nabla \times \mathbf{B} = \frac{\mathbf{j}}{\epsilon_0} \quad (2.2)$$

Magnetic fields aren't very intuitive for people because people cannot sense it or see it. It can be visualized in two dimensions but visualizing a vector field in three dimensions is difficult. It will, therefore, help to gain insight through the maths. If one considers equation 2.1, it states that the divergence of the magnetic flux density (\mathbf{B}) is equal to zero. This means that a magnetic field does not start from a "magnetic source" or stop.

Equation 2.2 states that the curl of the magnetic field (\mathbf{B}) is equal to the current density (\mathbf{j}) divided by the speed of light (c) squared and the permittivity of free space. What is important to note from the two equations, however, is that the equations represent a linear system in \mathbf{B} and \mathbf{j} . This means one can apply the superposition principle to magnetic fields. The significance of this will become clear when discussing permanent magnets.

The second important property of magnetic fields can be deduced by considering a magnetic dipole. A magnetic dipole can be considered as a magnetic "source" and is generally accepted as a small current loop. The reason it is referred to as a dipole is that the magnetic field produced by the dipole can be modeled as two magnetic monopoles of opposite signs, a small distance from each other. Although there is no such thing as a magnetic charge (monopole) and thus dipole, the model is a good assumption for modeling magnetic fields far away from a dipole. The magnetic field produced by such a dipole can be described by the equations 2.3 (Griffiths, 1999):

$$\mathbf{B}(\mathbf{r}) = \frac{\mu_0}{4\pi r^3} [3(\mathbf{m} \cdot \mathbf{r})\mathbf{r} - \mathbf{m}] \quad (2.3)$$

\mathbf{r} is the distance vector and \mathbf{m} the magnetic dipole moment vector.

This equation leads to the third important point. The magnetic flux density (\mathbf{B}) is twice on the axis of the dipole than perpendicular on the axis, the same distance away from the dipole. The axis of a dipole refers to a line through the two monopoles of the dipole. Furthermore, it is shown that the field depreciates cubically in distance from the dipole.

The last point of importance is the approximation of the magnetic dipole moment (\mathbf{m}). The magnetic dipole moment determines the magnetic flux density produced by the dipole over a distance. It can be approximated for a permanent magnet that is evenly magnetized to be:

$$\mathbf{m} \approx \frac{B_r * Volume}{\mu_0} \quad (2.4)$$

Where B_r [T] is the residual flux density, Volume [m^3] refers to the volume of the magnet and μ_0 the permeability of a vacuum. Permanent magnets are graded according to the maximum energy product (BH_{max}). The parameter of interest is, however, the residual flux density (B_r).

The magnetic flux density of the magnetic field produced will be proportional to the volume of the magnet with the same grade and shape (*EM GeoSci – Electromagnetic Geophysics*, no date).

In summary, the important characteristics of magnetic fields and permanent magnets in this project are:

- Magnetic field loop
- Superposition applies
- Double the strength of magnetic flux density on dipole axis
- The dipole moment is directly proportional to the volume of the permanent magnet with the same grade and shape

2.2.2 Magnetometers

This section discusses the theory of magnetometers as it relates to the project. A quick overview of the technology used is introduced, along with error modeling and calibration of magnetometers. The most common use for magnetometers is digital compasses. The error modeling and calibration theory were developed for digital compasses but fit into this project's application as well.

A magnetometer is a device capable of measuring the magnetic flux density of a magnetic field (Ramos and Ribeiro, 2014). Most of the magnetometers considered for this project is used in digital compasses. The most common of which is hall effect sensors.

The sensor used in the project is an inductive magnetometer. The sensor consists of an induction coil with a ferromagnetic core. The sensor functions on the principle of Faraday's law of induction (Forsmark, 2017).

The error modeling in this section follows the process described by Renaudin, Afzal, & Lachapelle (2010) for modeling magnetometer errors. Errors in magnetometers can be categorized into sensor errors and magnetic field errors. Sensor errors are due to manufacturing error or inherent in the type of sensor used. Magnetic field errors must be viewed in the context of the target measurement. If the target is to measure the earth's magnetic field, any ferromagnetic material or magnetic "source" (permanent magnet or electromagnet) will influence the measurement of the earth's magnetic field.

The discussion of errors is going to be in the context of the example above. The target is the earth's magnetic field. In a three-axis magnetometer, the expected result when measuring the earth's magnetic field will be a vector directed towards magnetic north with an origin at zero and magnitude of the earth's magnetic field at that specific location on earth.

Three types of sensor errors exist. The first is a scale error in the magnetometer. This will result in an increase in the size of the x, y and z components of the measured field.

If we consider \mathbf{B} the magnetometer measured vector and $\mathbf{B}_{\text{earth}}$ to be the earth's magnetic field vector, the scale error will deform as follows.

$$\mathbf{B} = \begin{bmatrix} B_x \\ B_y \\ B_z \end{bmatrix} \quad (2.5)$$

$$\mathbf{S} = \begin{bmatrix} S_x & 0 & 0 \\ 0 & S_y & 0 \\ 0 & 0 & S_z \end{bmatrix} \quad (2.6)$$

Resulting in an error model:

$$\mathbf{B} = \mathbf{S}\mathbf{B}_{\text{earth}}. \quad (2.7)$$

Figure 2 illustrates the transformation in the separate components of the vector measured and the earth's actual magnetic field vector.

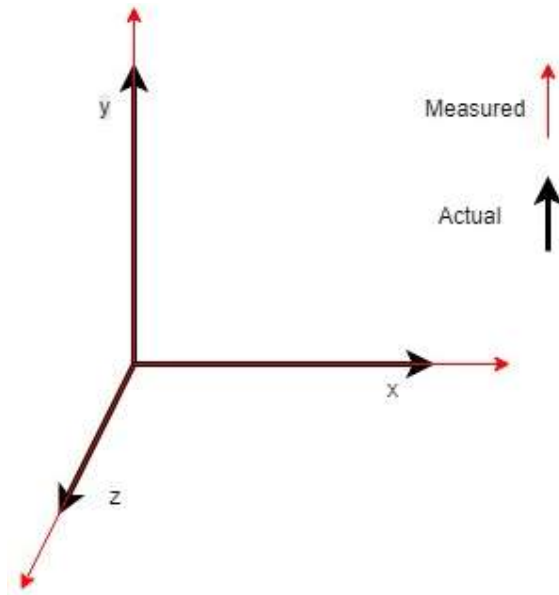


Figure 2: Scaling error

The second error is a misalignment error. This is when the x, y, and z-axis of the magnetometer is not orthogonal to each other. This error can be modeled as a matrix \mathbf{M} .

Where \mathbf{M} is the inverse of matrix \mathbf{N} . \mathbf{N} is a matrix that consists of column vectors that represent the misalignment of the sensor's axis relative to the frame of the sensor of reference:

$$\mathbf{M} = \mathbf{N}^{-1} \text{ And} \quad (2.8)$$

$$\mathbf{N} = [\mathbf{n}_x \quad \mathbf{n}_y \quad \mathbf{n}_z] \quad (2.9)$$

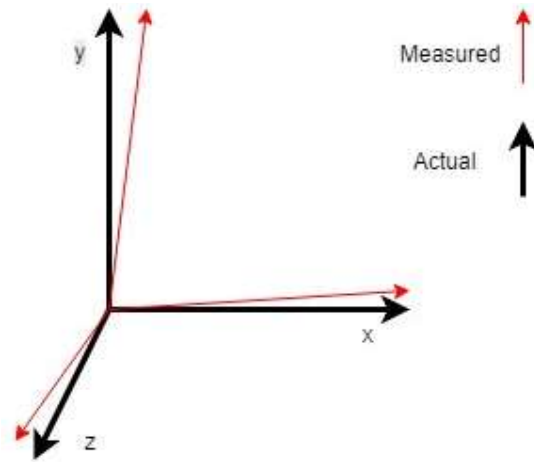


Figure 3: Misalignment error

The error model is now:

$$\mathbf{B} = \mathbf{SNB}_{\text{earth}} \quad (2.10)$$

The third sensor error is due to bias error. This will result in the origin of the measured field to shift. The error is modeled by adding a bias error (\mathbf{b}). The error model becomes:

$$\mathbf{B} = \mathbf{SNB}_{\text{earth}} + \mathbf{b} \quad (2.11)$$

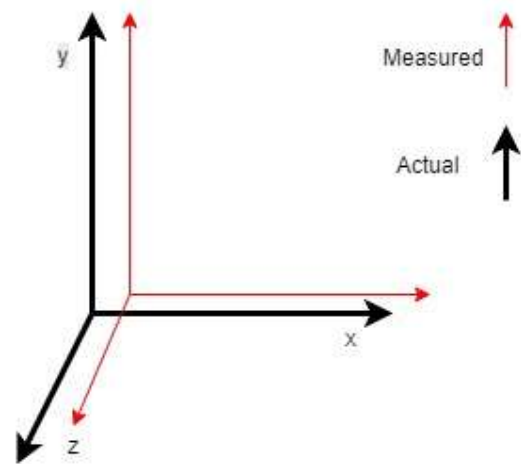


Figure 4: Bias error

Next are the magnetic field errors. There is two type of magnetic field errors. The first type is known as soft-iron errors. These errors are caused by ferromagnetic materials that have an induced magnetic field due to an external magnetic field. The error results in a distortion of the magnetic field resulting in the most complex error model. The errors are modeled as a full 3x3 matrix (**A**).

$$\mathbf{A} = \begin{bmatrix} a_{11} & a_{12} & a_{13} \\ a_{21} & a_{22} & a_{23} \\ a_{31} & a_{32} & a_{33} \end{bmatrix} \quad (2.12)$$

The full error model becomes:

$$\mathbf{B} = \mathbf{SN}(\mathbf{A}\mathbf{B}_{\text{earth}}) + \mathbf{b} \quad (2.13)$$

The second magnetic field error is known as hard-iron errors. The hard-iron errors are due to magnetic “sources” (excluding the earth’s magnetic field). The error produced is similar to the bias error. The vector will shift the origin. The error is again modeled by adding a bias vector (**b_e**). The complete error model for the magnetometer is:

$$\mathbf{B} = \mathbf{SN}(\mathbf{A}\mathbf{B}_{\text{earth}} + \mathbf{b}_e) + \mathbf{b} \quad (2.14)$$

The calibration of the magnetometer tries to eliminate the errors described in section 2.2.2.1. An established method to calibrate a magnetometer for navigation in digital compasses is a two-step process (*Teslabs Engineering - A way to calibrate a magnetometer*, no date). The process is easier to understand when described graphically. The error model described in section 2.2.2 can be simplified to equation 2.16 from equation 2.14:

$$\mathbf{B} = \mathbf{A}_{\text{new}}\mathbf{B}_{\text{earth}} + \mathbf{b}_{\text{new}} \quad (2.16)$$

A_{new} and **b_{new}** are the summarised parameters that are being determined. The target is **B_{earth}**. **B** is the measured magnetic flux vector from the sensor. Graphically it can be represented as:

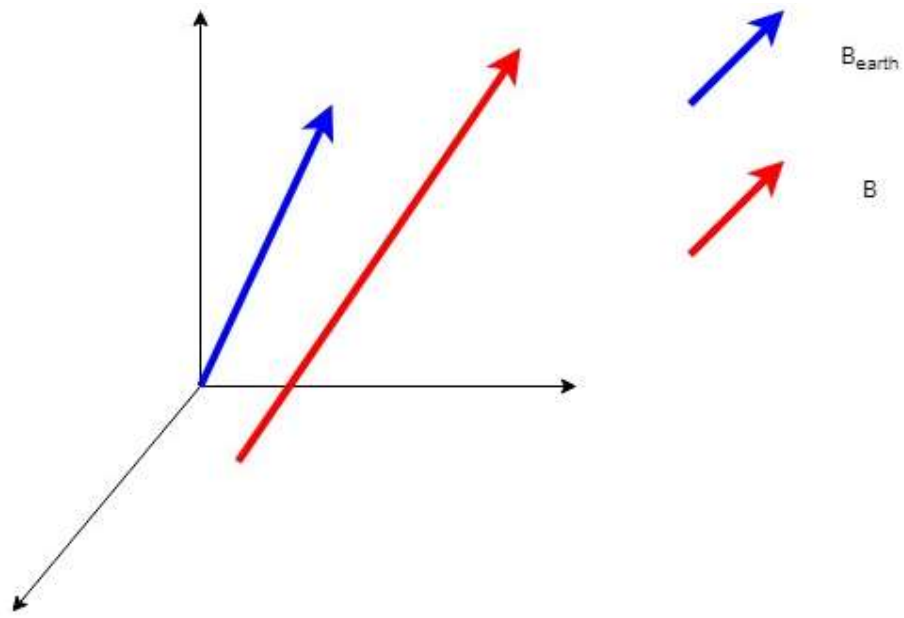


Figure 5: Actual and target magnetic flux density

\mathbf{A}_{new} elongates and changes the direction $\mathbf{B}_{\text{earth}}$. \mathbf{b}_{new} shifts the origin of vector $\mathbf{B}_{\text{earth}}$. The constants \mathbf{A}_{new} and \mathbf{b}_{new} cannot be determined from one vector \mathbf{B} . Multiple readings need to be taken. Plotting and connecting multiple readings in two-dimension at a different orientation of the magnetometer would result in an ellipse from the actual readings and a circle from the target readings. Figure 5 is discrete data points that are connected.

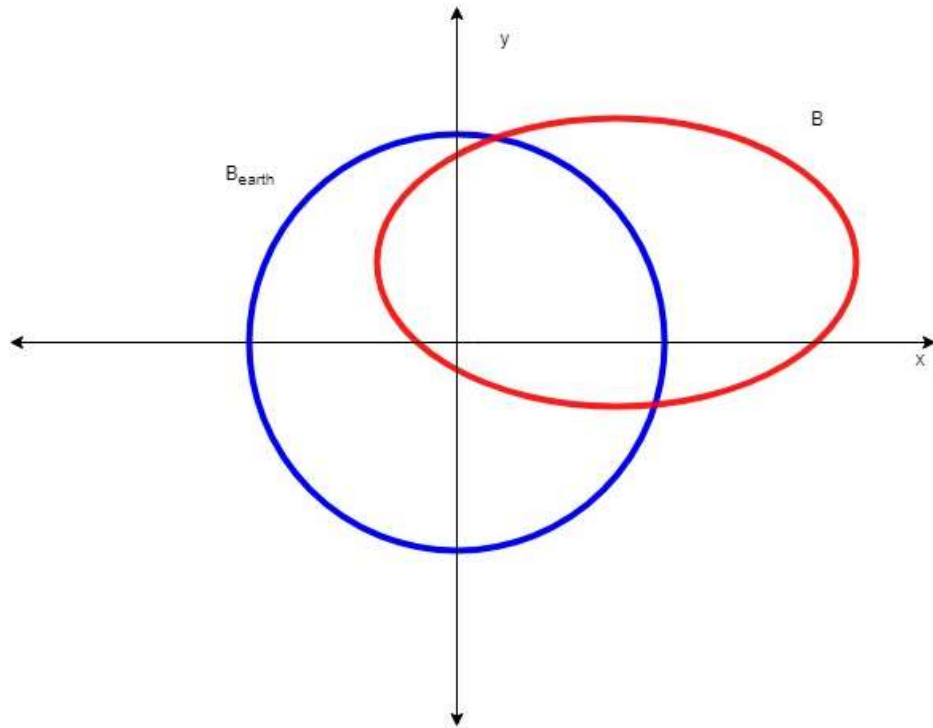


Figure 6: Multiple actual and target magnetic flux densities

The process to determine the constants are to first determine the parameters of the ellipse from the set of discrete data points. If an ellipse is fitted to the data points, the ellipse can be transformed to circle. In three dimensions the data must be fitted to an ellipsoidal and transformed to a sphere.

Using a process described by Li & Griffiths an ellipsoid was fitted to the data points (Qingde Li and Griffiths, 2004). The mathematical process is as follows:

Step 1: Calculate the parameters of an ellipse from the data points:

The general equation for an ellipsoid is:

$$ax^2 + by^2 + cz^2 + 2fxy + 2gxz + 2hxy + 2px + 2qy + 2rz + d = 0 \quad (2.17)$$

For each data point (i) in the data set (n) a vector (X) is defined:

$$\mathbf{X}_i = (x_i^2, y_i^2, z_i^2, 2x_i z_i, 2y_i z_i, 2x_i y_i, 2x_i, 2y_i, 2z_i, 1)^T \quad (2.18)$$

and the constants are:

$$\mathbf{v} = [a, b, c, f, g, h, p, q, r, d]^T \quad (2.19)$$

The least squares problem for the specific set are given by the following equation:

$$\min \|D\mathbf{v}\|^2 \quad (2.20)$$

and it is subjected to a constraint for an ellipsoid of:

$$\mathbf{v}^T \mathbf{I} \mathbf{v} = 1 \quad (2.21)$$

where D is defined as the design matrix of size 10*n:

$$\mathbf{D} = [X_1, X_2, X_3, \dots, X_n] \quad (2.22)$$

And J and I defined as:

$$I = a + b + c \quad (2.23)$$

$$J = ab + bc + ac - f^2 - g^2 - h^2 \quad (2.24)$$

Additionally, matrix C can be defined as a square matrix of size 10*10:

$$\mathbf{C} = \begin{bmatrix} C_1 & 0_{6 \times 4} \\ 0_{4 \times 6} & 0_{4 \times 4} \end{bmatrix} \quad (2.25)$$

Where C1 is defined:

$$\mathbf{C}_1 = \begin{bmatrix} -1 & \frac{k}{2} - 1 & \frac{k}{2} - 1 & 0 & 0 & 0 \\ \frac{k}{2} - 1 & -1 & \frac{k}{2} - 1 & 0 & 0 & 0 \\ \frac{k}{2} - 1 & \frac{k}{2} - 1 & -1 & 0 & 0 & 0 \\ 0 & 0 & 0 & -k & 0 & 0 \\ 0 & 0 & 0 & 0 & -k & 0 \\ 0 & 0 & 0 & 0 & 0 & -k \end{bmatrix} \quad (2.26)$$

The constraint can be restated as:

$$\mathbf{v}^T \mathbf{C} \mathbf{v} = 1 \quad (2.27)$$

The minimization problem can be solved with solving the following set of equations with LaGrange multipliers:

$$\mathbf{D} \mathbf{D}^T \mathbf{v} = \lambda \mathbf{C} \mathbf{v} \quad (2.28)$$

$$\mathbf{v}^T \mathbf{C} \mathbf{v} = 1 \quad (2.29)$$

K = 4 for an ellipsoid:

$$\mathbf{D}\mathbf{D}^T = \begin{bmatrix} S_{11} & S_{21} \\ S_{12}^T & S_{22} \end{bmatrix} \quad (2.30)$$

$$\mathbf{v} = \begin{bmatrix} \mathbf{v}_1 \\ \mathbf{v}_2 \end{bmatrix} \quad (2.31)$$

\mathbf{v}_1 has a length of six and \mathbf{v}_2 has a length of 4. The eigenvalue system that needs to be solved can be reduced by substituting \mathbf{v}_2 into equation (above).

$$\mathbf{v}_2 = -S_{22}^{-1}S_{12}^T \mathbf{v}_1 \quad (2.32)$$

$$C^{-1}(S_{11} - S_{12}S_{22}^{-1}S_{12}^T)\mathbf{v}_1 = \lambda\mathbf{v}_1 \quad (2.33)$$

The eigenvectors of \mathbf{v}_1 and \mathbf{v}_2 relate to \mathbf{v} in the following manner:

$$\mathbf{v}_1 = (a, b, c, f, g, h)^T \quad (2.34)$$

$$\mathbf{v}_2 = (p, q, r, j)^T \quad (2.35)$$

The center of the ellipsoid can be calculated by setting up matrix \mathbf{Q} and \mathbf{U} :

$$\mathbf{Q} = \begin{bmatrix} a & f & g \\ f & b & h \\ g & h & c \end{bmatrix} \quad (2.36)$$

$$\mathbf{U} = \begin{bmatrix} p \\ q \\ r \end{bmatrix} \quad (2.37)$$

The center of the ellipsoid is calculated using equation (below):

$$\mathbf{b}_{\text{new}} = -\mathbf{Q}^{-1}\mathbf{U} \quad (2.38)$$

The constants for an ellipsoid and the center of the ellipsoid is determined.

Step 2: Transform the ellipsoid into a sphere:

The next step is to transform the ellipsoid into a sphere by calculating the A_{new} constant. The A_{new} constant can be calculated using the following equation (Renaudin, Afzal and Lachapelle, 2010):

$$\mathbf{A}_{\text{new}}^{-1} = \frac{r}{\sqrt{\mathbf{b}_{\text{new}}^T \mathbf{Q} \mathbf{b}_{\text{new}}}} \mathbf{Q}^{1/2} \quad (2.39)$$

Where the r is the radius of the sphere. The calculated \mathbf{A}_{new} and \mathbf{b}_{new} can be multiplied with each data point in the data set to transform the data set.

2.2.3 Magnetometer axis alignment with Single value decomposition

The algorithm is used to align the two magnetometer axes which are fixed relative to each other. The implementation of the algorithm is discussed further in chapter 4.

The method used was used by Besl and McKay (Besl and McKay, 1992) for finding the best translation and rotation between the two corresponding 3-dimensional datasets. The method calculates a single value decomposition (SVD) to determine a rotation matrix through which one set is transformed with.

Consider transforming dataset E_2 to E_1 . Both have N amount of rows. First, calculate H :

$$\mathbf{H} = \sum_{i=1}^N \mathbf{E}_{1i}(\mathbf{E}_{2i})^T \quad (2.40)$$

Next, take the SVD of H to calculate U , S , and V :

$$[\mathbf{U}, \mathbf{S}, \mathbf{G}] = \text{svd}(\mathbf{H}) \quad (2.41)$$

Calculate matrix R , the rotational matrix through which the dataset B_2 will be transformed by.

$$\mathbf{R} = \mathbf{G}\mathbf{U}^T \quad (2.42)$$

Dataset B_2 is transformed by multiplying R with B_2 .

$$\mathbf{B}_{2\text{transformed}} = \mathbf{R}\mathbf{B}_2 \quad (2.43)$$

Aligning two magnetometers to the same coordinate system can also be solved by this algorithm. If one would measure the earth's magnetic field with both magnetometers, one can transform the magnetometers data towards the other magnetometers coordinate system. The reason for this is both magnetometers are measuring the same field with different orientations. The two datasets are theoretically the same but at different orientations.

2.3 Machine learning

Machine learning can be broadly categorized into two categories: Supervised and unsupervised learning. Supervised learning is a learning problem where the data comes with the features that need to be predicted (Pedregosa *et al.*, 2011; Géron, 2017). Another explanation of this is, one trains one's algorithm with a dataset and the labels, and then the algorithm predicts the labels of unseen data. Unsupervised learning is when one gives the algorithm a set of input data without specified labels (Pedregosa *et al.*, 2011). The algorithm then sorts the similar data into groups. This project is going to focus on supervised learning.

Another way to categorize machine learning is to consider instance-based learning and model-based learning. The instance-based learning algorithms function by determining the similarity of a new data point in relation to the trained examples. Figure 7 illustrates this. The new instance measures the “similarity” which is, in this case, the distance to the two nearest trained examples. The algorithm then predicts the class the new instance belongs to.

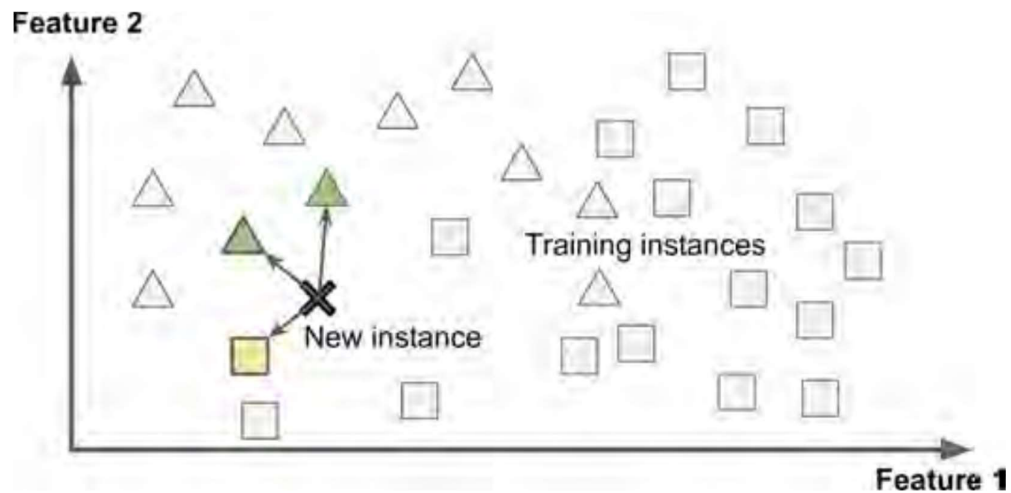


Figure 7: Instance-based learning (Géron, 2017)

Model-based learning is more commonly used in engineering. A linear model line fit to data is the simplest example of a model-based learning algorithm. In figure 8 a “boundary” or the model is drawn with the dotted line. The model is set up on the training data and the new instance is classified according to which side of the line it falls.

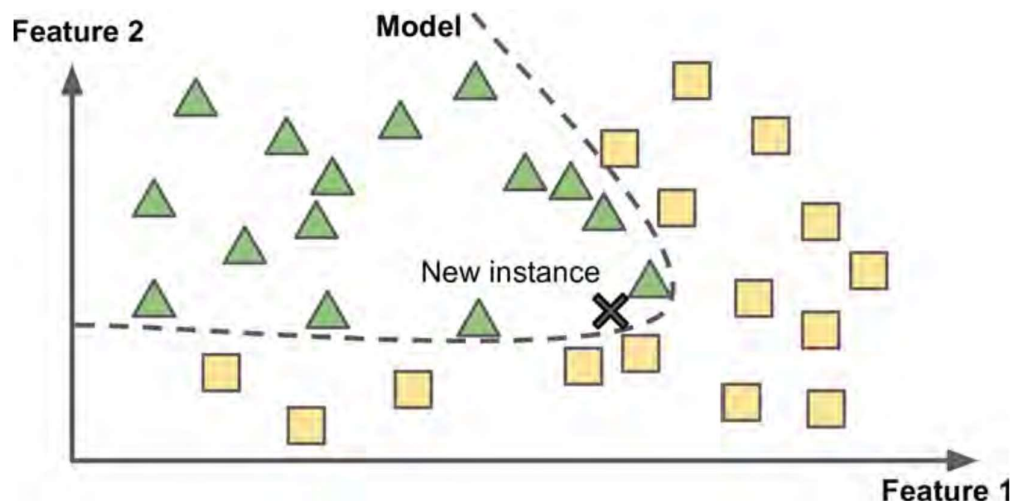


Figure 8: Model-based learning (Géron, 2017)

2.3.1 General model evaluation

Evaluating a machine learning model is a difficult task. The first logical step is to set performance measures to which the model will be evaluated against. These performance measures are problem dependent. A common challenge is to avoid overfitting the data and essentially start fitting the noise in the data (Géron, 2017). This is considered memorizing and not learning.

In other words, overfitting is when a too complex a model is chosen for the problem. Overfitting can be explained at the hand of variance and bias. Variance is how sensitive the model is to a varying training set (Pedregosa *et al.*, 2011). Bias is the average error for different training sets (Pedregosa *et al.*, 2011). An overfitted model will have a high variance and low bias, while an under fitted model will have a high bias and low variance. There is always a trade-off between bias and variance. Evaluating models comes down to finding the appropriate trade-off between the two. The goal of a good model is to achieve an average error that is only a measurement of the noise in the data and a low possible bias and variance.

Evaluating models to achieve the optimal variance and bias trade-off with a low average error can be done with evaluating two plots: the validation curve and learning curve. The validation curve is an accuracy score for the model plotted against the model complexity. Two accuracy scores are plotted on this curve. The in-sample accuracy score and the out of sample accuracy score. Out of sample accuracy score is determined by splitting the dataset into a training and testing set. The model is trained on the training set and tested on the test set to determine the accuracy score. The rule-of-thumb for the split between the training and test

sets are usually 80/20 (Géron, 2017). In-sample accuracy is an accuracy score when the model is tested on the data used for training.

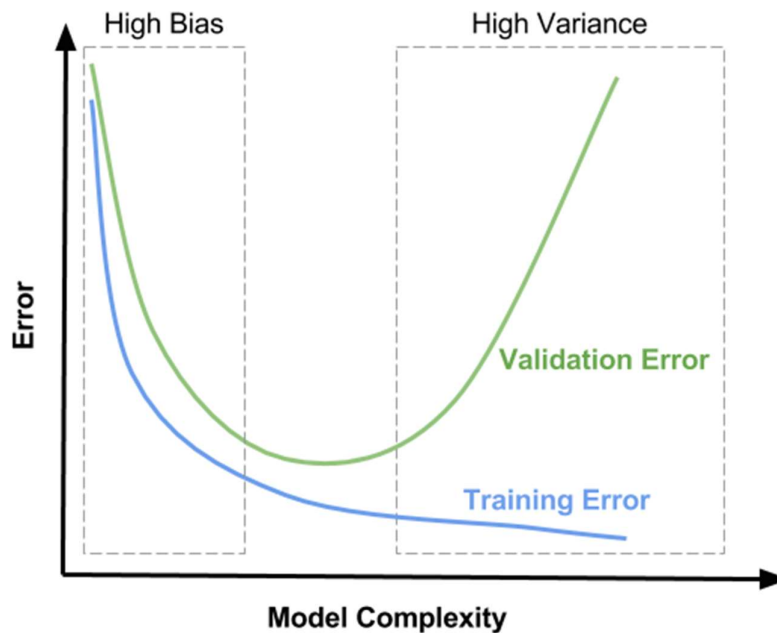


Figure 9: Validation curve (Géron, 2017)

The validation curve helps to evaluate the optimal complexity of the model for the data provided. A good model complexity is where the validation score reaches a maximum or the validation error reaches a minimum.

The second plot to evaluate the model is the learning curve. It is a plot of the accuracy score plotted against the number of training examples for training accuracy and validation accuracy. The plot provides insight into the amount of data needed to achieve a low variance and bias. In a good model, the accuracy score for both the training score and the validation score will converge to the same accuracy score. The accuracy score it converges to is important. If a model converges it may not be the optimal model, it only states the number of training examples is sufficient to achieve an optimal bias and variance trade-off for the specific model. Figure 10 is a sample of a learning curve.

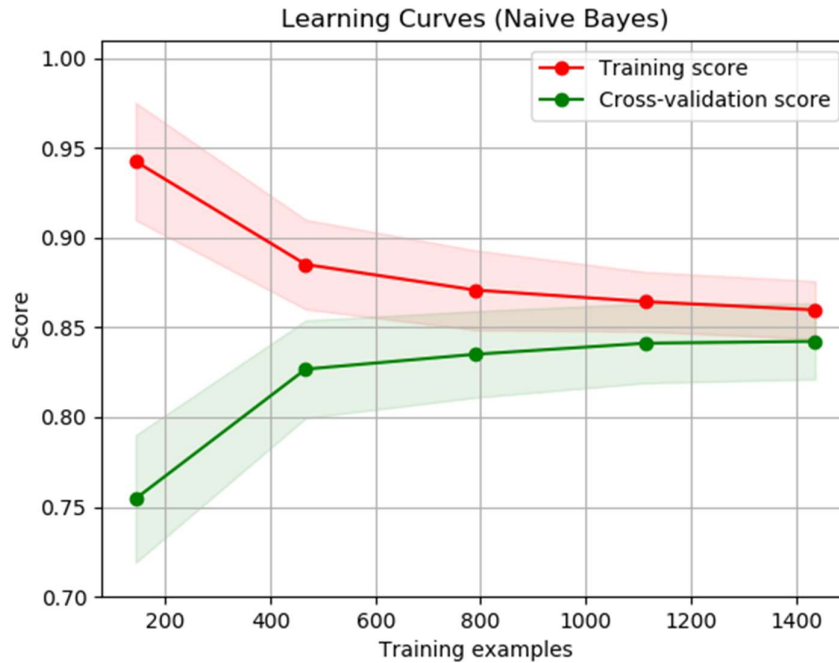


Figure 10: Learning curve (Pedregosa *et al.*, 2011)

The next performance measurement focusses on classification models and is called a confusion matrix. A confusion matrix is a 2-dimensional matrix that compares the predicted labels with the actual labels. The columns are the predicted labels and the actual labels are the rows. Each tested instance is placed in the matrix. If the instance is predicted in the right class, it will fall on the diagonal. If the instance is predicted in the wrong class, it will be in the column of predicted class and the row of the true class. The instance will fall off-diagonal in the matrix. Table 1 is an example and an explanation of a confusion matrix

Table 1: Confusion matrix

		ACTUAL	
		Positive	Negative
PREDICTED	Positive	True positive	False positive
	Negative	False negative	True Negative

2.3.2 K-Nearest neighbours

K-nearest neighbours (k-NN) is an instance-based model. The model is generally used for classification but can be used for regression purposes too. k-NN classification functions, in simple terms, is calculating the k-nearest points by distance in a multidimensional space. The method for calculating the distance can be changed but the most common is the Euclidian distance between two points. The new instance will be classified with the label that has the majority out of the k-number of neighbours.

Other parameters that can be tuned are the weighting of the data points and the algorithm used to calculate the nearest neighbours. Weighting can either be done linearly or inversely proportional to the distance away from the new instance. Weighting the data inversely will cause data points closer to the instance to have a more significant influence.

K-NN regression function in a similar manner to classification but rather than classifying according to the nearest neighbours, the model takes an average of the k-nearest neighbours to predict the value of the new instance.

Important caveats to note for k-NN are: The features must be scaled otherwise a feature with a different numerical scale may have a larger or smaller influence on the predicted data. K-NN also doesn't handle multi-dimensional data well.

2.4 Human joint coordinate system

The International Society of Biomechanics recommends using the following angles for measuring hip joint angles ('ISB recommendation on joint coordinate', 2002). The hip angles are defined using the pelvic and femoral coordinate system. The pelvic coordinate system is defined as follows:

- O: The center of rotation of the hip
- Z: The line parallel to a line connecting the right and left anterior superior iliac spines (ASIS) and pointing to the right.
- X: The line parallel to a line lying in the plane defined by the two ASIS and the midpoint of the two PSISs, orthogonal to the Z-axis, and pointing anteriorly.
- Y: The line perpendicular to both X and Z

The femoral coordinate system is defined as:

- o: The origin coincident with the right (or left) hip center of rotation, coincident with that of the pelvic coordinate system (O) in the neutral configuration.
- y: The line joining the midpoint between the medial and lateral FEs and the origin and pointing cranially.
- z: The line perpendicular to the y-axis, lying in the plane defined by the origin and the two FEs, pointing to the right.
- x: The line perpendicular to both y- and z-axis, pointing anteriorly

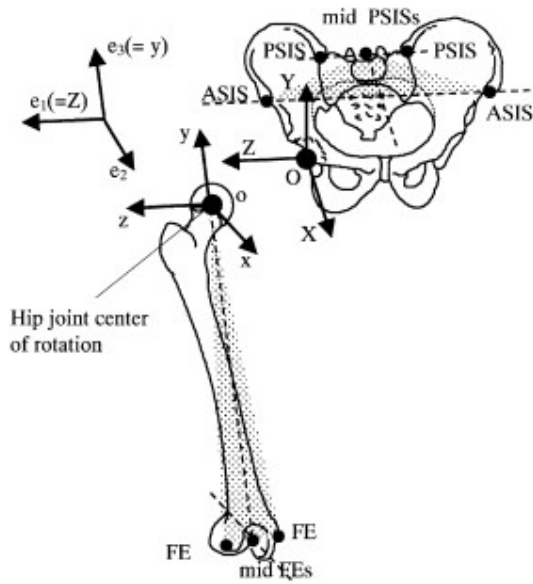


Figure 11: The femoral and pelvic coordinate system (“ISB recommendation on definitions of joint coordinate system”, 2002)

The important section for this project is the joint coordinate system for the hip joint.

- e₁: The axis aligns with the Z-axis of the pelvic coordinate system. The rotation around the axis is flexion or extension.
- e₃: The axis aligns with the y-axis of the femoral axis system. The rotation around the axis is known as internal and external rotation.
- e₂: The axis is perpendicular to e₁ and e₃. The rotation around this axis is known as the abduction and adduction.

3 Device design

A system engineering approach was followed to design the device. This method was selected because of the complexity of the device and the multiple design variables involved.

The systems engineering approach, as described by Blanchard and Fabrycky (2014), has the following workflow illustrated in figure 12. In this project, the researcher only focused on completing the first level of the approach namely: Conceptual design and Preliminary design. The rest of the system approach is not applicable to the project due to budget constraints.

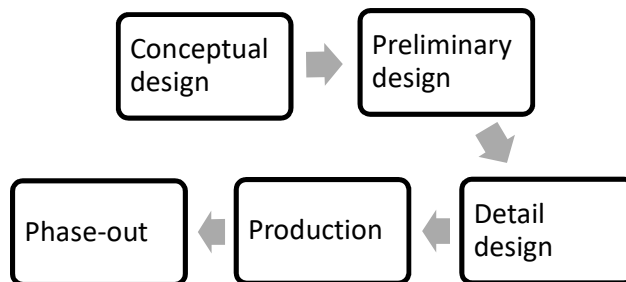


Figure 12: Systems engineering approach

Each step in the systems engineering approach can be further broken down into sub-sections. This section discusses in detail each step in the conceptual design and preliminary design.

3.1 Conceptual design

The conceptual design processes are discussed in this section. The conceptual design process is described in more detail in figure 13.

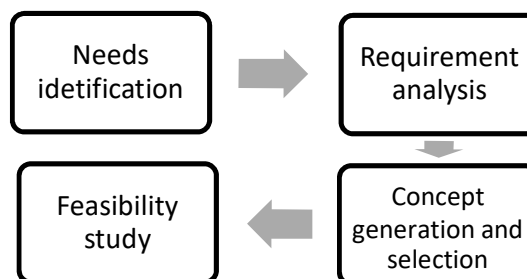


Figure 13: Conceptual design

3.1.1 Needs identification

The needs identification of the device was developed by taking into account the client's needs for the device and reviewing the relevant literature in the field of hip impingement. The main need is to build a device that is capable of determining if an individual reaches a specific hip position during sports. The client concluded the device should for fill the following needs.

- The device must be robust enough to endure the requirements of a sports game and ultimately withstand the demands of a rugby match.
- The device should not inhibit the athlete in any way to perform the sport.
- The device should be accurate for a long period of time, up to but not limited to 24 h.
- The device should be able to operate outside a lab environment and be used on a sports field.

3.1.2 Requirement analysis

The requirement analysis section gives support to the final requirement stated in section 1.3. The rationale of determining the requirements from the customer's needs is discussed in this section.

All the requirements are not fully for filled in this project, but design decisions had to be made to for fill all the requirements when the device is going to be fully developed. In a proof of concept, only sufficient evidence needs to be given that the device is capable of meeting the requirements in the final, detail design phase.

- **Robustness:** The need relates to the technology chosen for the concept. The concept needs to be robust or it needs to be encapsulated to make it robust. The device is ultimately required to pass the IP 67 standard from the International Protection Rating for electrical enclosures. The standard is in accordance with International Electrotechnical Commission (IEC) 60529 code. The design decision is based on the enclosure protection of a commercial heart rate straps IP code currently used in rugby. The design of the enclosure is not in the scope of the project, but the device must thus only be capable of being fully enclosed. The device should also be able to ultimately endure a rugby match.
- **User-friendly in use:** This can only be subjectively measured and not quantified. The requirement was assessed by asking the participant in the pilot study if the device was uncomfortable or inhibited the movements performed.

- Accuracy: A hip morphology related range of motion restriction smaller than 5 ° in the hip joint is not considered as a major restriction of the hip joint (Röling *et al.*, 2015). If the hip joint can reach an end range of motion within 5 ° the patient won't be considered to have severe hip impingement morphology. The device in development needs to detect if a person reaches a specific position within the 5 ° threshold in all three directions of freedom of the hip joint

The device should also be accurate when used in impact sports, for example, rugby.

- The device should be able to operate outside of a lab environment. The requirement can simply be tested outside with a binary outcome.

3.1.3 Concept generation and selection

Two concepts were generated. The concepts were generated to best meet the needs and requirements. Each concept is discussed in this section. The first concept is an IMU system that consists of IMU sensors on the pelvis and on the femur to measure the relative angle between the femur and the pelvis. This approach was already followed in multiple studies and it is an established method to measure hip angles (Cockcroft, 2015).

The second concept was based on research done by (Bianchi and Oakley, 2015). Bianchi & Oakley created interactive toys using magnetic tracking of a rotating permanent magnet. The sensing was done by a magnetometer on a mobile device. The novel part of their research was that the toys could be used for many functions and didn't need to be pre-trained. The training was done by the user and facilitated by a machine learning algorithm. The research by Bianchi and Oakley established the base of the idea the of the machine learning calibrated, permanent magnet motion tracking device.

Following on the research done by Bianchi and Oakley, a permanent magnetic tracker can function as a hip angle position tracker if the permanent magnet is placed on the thigh and the magnetometer/s is placed on the pelvis, thus tracking the relative angle of the hip.

3.1.4 Feasibility study

The feasibility study consists of a review of the literature and a simple experiment to determine whether the concepts are likely to meet the needs and requirements established.

Firstly, the IMU-based concept will be discussed. The literature review revealed shortcomings in the technology for the application proposed in the project. The most significant shortcoming is the effect drift. As previously mentioned in section

2.1, the problem can be overcome with an adequate biomechanical model. The model, however, increases the complexity in setting up the sensors. The most significant shortcoming is the effect of impact sports on the inertia-based sensors. The effect of the impact on the sensors is unknown.

Due to the lack of literature regarding magnetic position tracking the researcher conducted an experiment to determine if the concept is feasible. The experiment's aim was to test the accuracy of classifying the location of a permanent magnet over a distance with a machine learning algorithm. The experiment was set up with an Arduino UNO (Arduino LLC, Italy) as a data acquisition system for a MAG3110 magnetometer from Freescale semiconductors (Austin, USA). The magnetometer had a sensitivity of $0,1 \mu\text{T}$ and a range of $1000 \mu\text{T}$. The permanent magnet used was an N38 neodymium magnet with a 20 mm diameter and a width of 5 mm. The flux density produced was $1,17 \text{ T}$ and the energy product 263 KJ/m^3 .

The protocol was to place the magnet at 10 locations on a straight line away from the magnetometer, starting at 500 mm and moving 20 mm closer with each position. The maximum distance was determined by considering that the magnet would not be further away from the magnetometer than the average length of a human femur. The 20mm interval was selected because the diameter of the magnet was 20mm. By using equation 2.3 and 2.4 in one dimension, the magnetic flux density of the magnetic field produced by the magnet would be around $3.96 \mu\text{T}$, because equation 2.4 is only an approximation.

Fifty samples were taken at each location. The process was repeated 10 times. The data was then shuffled and split 80/20 into training and testing sets. The machine learning algorithm used was Scikit-learns k-NN classification (Pedregosa *et al.*, 2011) with the default of 5 neighbours. The algorithm predicted with 100% accuracy the location of the magnet up to a distance of 460 mm. The experiment proved that a machine learning classification for the location of a permanent magnet by measuring the magnetic flux density is a feasible idea.

In table 2 the two concepts are compared to the requirements. The IMU concept is evaluated based on the literature and the magnetometer and permanent magnet concept is evaluated based on the feasibility experiment.

Table 2: Feasibility study

REQUIREMENT	IMU	MAGNETOMETER AND PERMANENT MAGNET
ACCURACY	<p>The required accuracy is achievable, as shown by López-Nava and Muñoz-Meléndez (2016) in multiple studies. The added complexity to remove the drift is a concern.</p> <p>The biggest concern is the unknown effect that impact would have on the inertia based sensors.</p>	<p>There is not sufficient evidence in the literature to estimate accuracy. The feasibility experiment proved the concept could possibly work with a more sensitive sensor and a larger magnet</p>
USER-FRIENDLY IN USE	<p>Commercially available systems require an IMU unit on the hip and thigh if hip angles are measured (Chepers, Giuberti and Bellusci, 2018). This can make the device more uncomfortable when compared to the magnetometer-based concept that only needs sensors on the pelvis.</p>	<p>There is not sufficient evidence in the literature to estimate if the device will be user-friendly.</p> <p>The concept can however, be compared to the IMU concept. The device should be more user-friendly because fewer sensors are used and the sensors are only located on the pelvis</p>
STAND-ALONE DEVICE	<p>The device can operate as a standalone device.</p>	<p>The device will be able to operate as a standalone device.</p>
ROBUSTNESS	<p>The device can be encapsulated to be made robust</p>	<p>The device can be encapsulated to be made robust. The device should be more robust than the IMU because fewer sensors are used, and the sensors are only located on the pelvis.</p>

The researcher concluded the magnetometer and permanent magnet concept better suit the requirements of the device. There are a lot of unknowns because the technology is not as mature as the IMU-based solution. The IMU concept was not chosen because of the concern over the effect the impact sports would have on the accuracy and specifically the drift in the device.

3.2 Preliminary design

The preliminary design phase in systems engineering is illustrated in figure 14. The next step, after the conceptual design, is to perform a functional analysis. The functional analysis could also be performed at the conceptual phase but the researcher decided it aids more in designing the sub-systems than selecting a concept.

Synthesizing and allocating the design criteria to the functions in the functional analysis helps the researcher to focus on each individual element of the design. The system and subsystem analysis are set out to establish the requirements of each subsystem. Lastly, the whole system is analyzed to evaluate the interaction between the sub-systems.

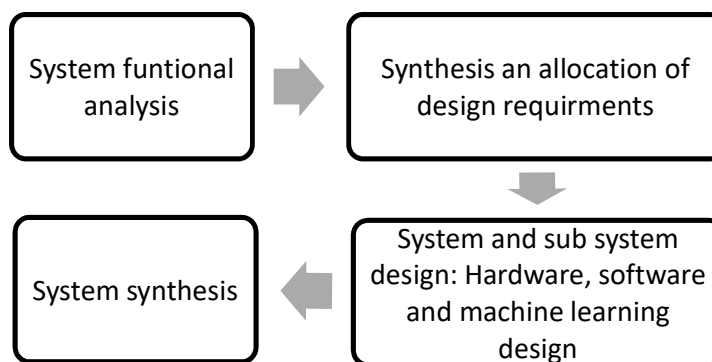


Figure 14: Preliminary design process

The system functional analysis was performed on the selected concept. The allocation of systems to a set of functions was also discussed in this section. The final device consists of a permanent magnet, three three-axis magnetometers, an IMU module and a central processing unit with a lithium polymer (LiPo) battery as power supply. The permanent magnet was placed in the middle of the thigh, while the sensors were placed on the upper part of the hip. The central processing unit was placed around the waist for testing but can be placed anywhere on the body. The position of the central unit can be changed depending on the sport.

The device functions in a three-step process. Firstly, the algorithm needs to be trained. This process creates the link between the hip position and the magnetic flux density signal from the sensors.

This process is followed to set the points of interest and set points not of interest. The patient will lie on their back while the doctor marks the points of interest and normal points with an application on a computer. The doctor will literally position

the hip to the point of interest and select on the application that it is a point of interest. The patient will then move his/her hip normally for about a minute to set the points that are not of interest. The training data is processed after the training to determine if the training is done successfully. Next, the device can be used to track the point of interest and be disconnected from the computer to use. The data will be recorded on an SD card in the central processing unit.

The whole process is explained visually in figure 15. The process is divided into two sections. The actions that are done to the patient and the actions that need to be completed on the computer through the application.

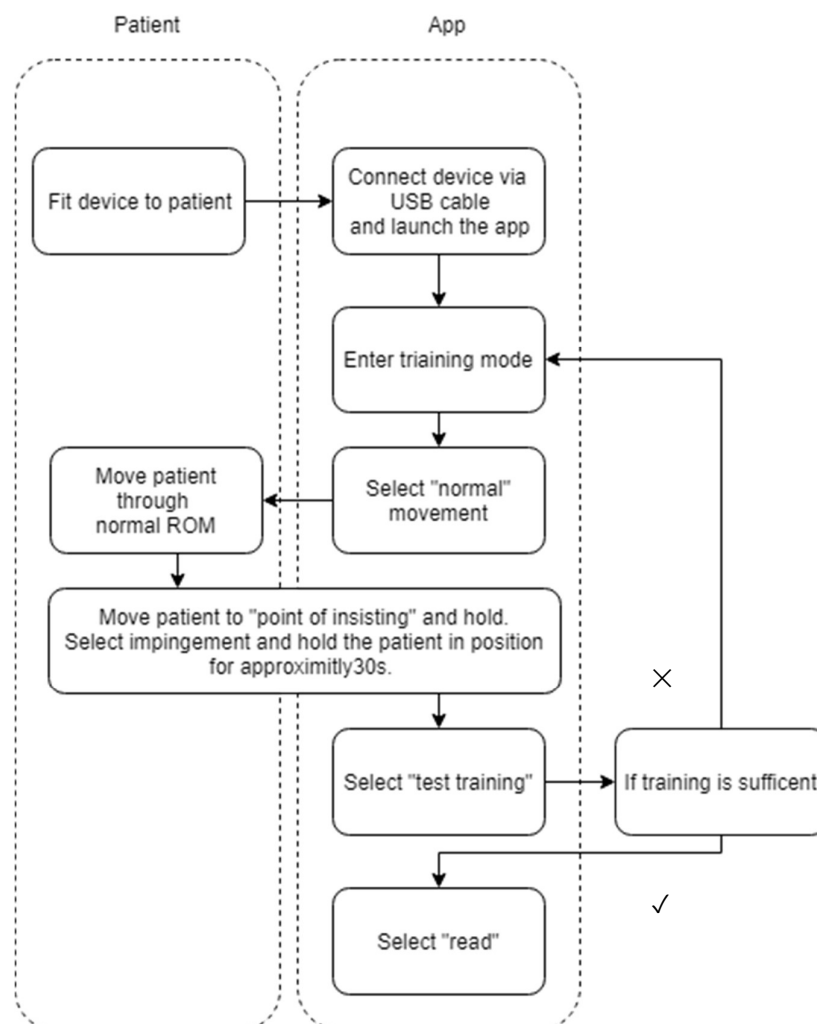


Figure 15: Device function

Lastly, when the patient is done with the activities, the data can be downloaded from the device to be run through the machine learning algorithm to detect the

points of interest instances in time. The output will be a plot displaying the percentage of nearest neighbours points of interest versus time. The output will be further discussed in section 3 in conjunction with the machine learning algorithm to better understand the output.

The functional analysis helped the researcher to divide the device into systems with allocated functions. From figure 15, the following systems were identified: Signal generation, data acquisition and storing, user interface and data processing and visualization. Table 3 shows how each system is allocated to specific hardware and software systems. The researcher decided it is more logical to divide the systems into hardware and software sections. Sections 3.3 to 3.6 discusses each system separately.

Table 3: System allocation

SYSTEM	HARDWARE	SOFTWARE
SIGNAL GENERATION	Magnet	Not applicable
DATA ACQUISITION AND STORING	Magnetometer	Sensor library
	Microcontroller	Microcontroller code
DATA PROCESSING	Computer	Data processing software
USER INTERFACE	Computer	Graphical user interface
DATA PROCESSING AND VISUALIZING	Computer	Machine learning
		Data visualizing code

3.3 Hardware design

The hardware selection was made by evaluating different options. The hardware selected for the final device best met the requirements that were set out.

3.3.1 Central unit

The central processing unit selected is Adafruit's feather M0 Adalogger microcontroller module ('www.adafruit.com', no date). The module consists of an ARM Cortex M0 48MHz processor, a battery JST connector cable for charging the battery, a micro-USB connection and a built-in microSD reader. The specific

microcontroller was chosen for several reasons. The already PCB mounted SD card reader and integrated battery charging were key factors in the choice.

3.3.2 Magnetometers

PNI's RM3100 magnetometer breakout board was selected (PNI Corporation, 2016). The sensor is an inductive magnetometer. The breakout board consists of three sensor coils, MagI2C ASIC controller and the necessary resistors and capacitors. The sensor is capable of communicating through Serial Peripheral Interface (SPI) or Inter-integrated Circuit (I²C) protocols. I²C communication was used in this project because this allows multiple magnetometers on the same SCL (serial clock line) and SDA (serial data line) lines. Figure 16 shows the pins available and the layout of the breakout board.

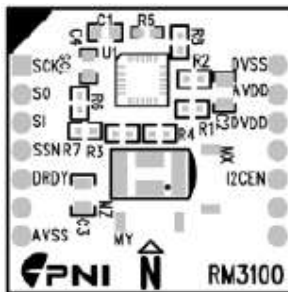


Figure 16: RM3100 magnetometer (PNI Corporation, 2016)

The AVSS pin was connected to ground and 3.3 V was supplied to the AVDD pin. I2C protocol was selected by pulling the I2CEN pin high. The breakout board can be configured for four different I2C 7-bit slave addresses. The slave address can be changed by pulling the SA0 pin and/or the SA1 pin high or low. Pin SA0 represents the least significant bit in the slave address and SA1 represents the second least significant bit. There are thus four unique possible combinations of slave addresses.

The reason for selecting this specific sensor is the maximum sampling rate of the sensor is 545 Hz. The sacrifice for the large sampling rate is an increase in size compared to smaller, Hall Effect sensor like the MAG3110 (Freescale Semiconductor, 2013). The increase in sampling frequency was, however, more important than an increase in the size of the sensors.

3.3.3 Magnets

Nine cylindrically shaped N38 neodymium magnets were used. Each magnet has a diameter of 6.25mm and a length of 25.4mm. The magnets were arranged in three rows, with five magnets in a row.

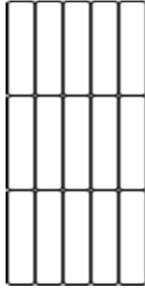


Figure 17: Magnet layout (not to scale)

The layout of the magnets was chosen such that the dipole axis points to the magnetometers. As discussed in section 2, the most significant characteristics of the magnet is the total volume. The volume of all the magnets combined is 4489 mm³.

3.3.4 IMU

The selection of the IMU was based on a combination of accuracy and availability. There are many “ready to use” IMU’s on the market. The one selected had a library already written and the reported accuracy was acceptable to the researcher. According to the manufacturer, the dynamic and static orientation accuracies are 3.5 ° and 2.0 ° respectively (excluding for heading). The heading, however, does have a drift of 0.5 °/h. The device selected was Hillcrest labs’ BNO080 sensor and the breakout board was produced by Sparkfun. The IMU consists of a three-axis gyroscope, accelerometer, and magnetometer. The data from these three sensors are processed by an ARM Cortex-M0+ microcontroller. The microcontroller is preprogrammed with Hillcrests SH-2 firmware. The firmware processes the sensor data through a sensor fusion algorithm and produces many outputs. The IMU can be used as an activity classifier, orientation tracker or the raw data can be requested from the sensors.

The raw data used in this project is referred to by the manufacturer as the “gaming rotational vector”. It is the orientation of the device expressed in quaternions. The orientation is calculated from only the accelerometer and gyroscope and processed by the microcontroller to produce the orientation angles. Note that a magnetometer is not used in the calculation of the orientation.

3.4 Software design

The software consists of three elements. The Arduino code together with the sensor libraries, the Python data-processing code and the Kivy and Python GUI (graphical user interface) code.

The Arduino code (C or C++ code) was written in the Arduino IDE (interactive development environment). The code had two functions. First to read the magnetometers data and save it to an SD card. Secondly to read both the magnetometer data and IMU data and send it through the serial port to a computer which is running the GUI. The user commands the microcontroller through the GUI.

The Kivy and Python GUI code was written for easy data-capturing. The Python data-processing code was used to implement the machine learning algorithms and display the processed data.

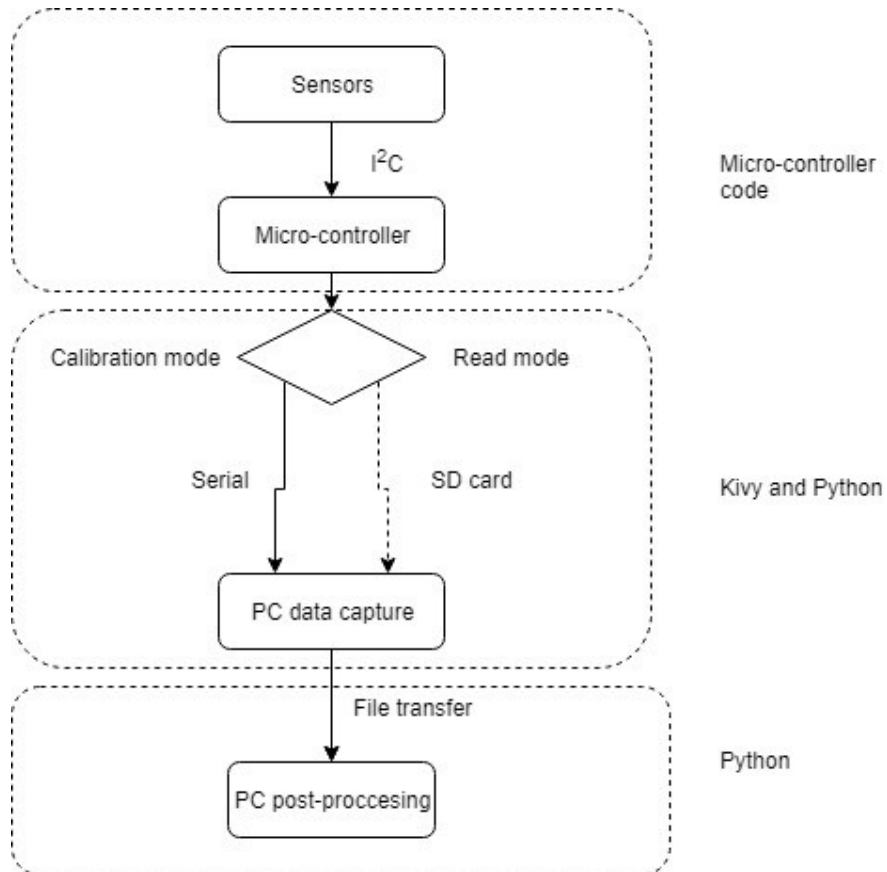


Figure 18: Software interactions

3.4.1 Microcontroller code

The Arduino code consists of two sections. The setup code that executes when switched on, and the loop code, that repeats or loops.

Figure 19 shows the Arduino logic flow diagram. The first step is the “Setup”. All the variables are initialized, and the sensors’ communication is established. The SD card is set up and serial communication is set up.

The microcontroller then enters the looped section of the code. The microcontroller reads the serial port and checks if either “read”, “calibrate” or “save” mode is activated.

If the “read” mode is selected, the “read” function is executed. The “read” function executes until a user input is received. The “read” function, only reads the two magnetometers and saves the result on an SD card. To stop the read function, one can connect the microcontroller to the computer and send the appropriate user-command. If for some reason the microcontroller loses power or stops working, the data will be saved on the SD card.

The “train” function also continues until a user input is received. The “calibration” functions read both magnetometers and the IMU for each iteration and send the result to the PC through which serial communication is established. The “save” function can be used to save the magnetometers data once done. The filename to which it must be saved on can be specified by the user. The “pause” function pauses the reading of any data. The logic of the whole process is explained in detail in figure 19.

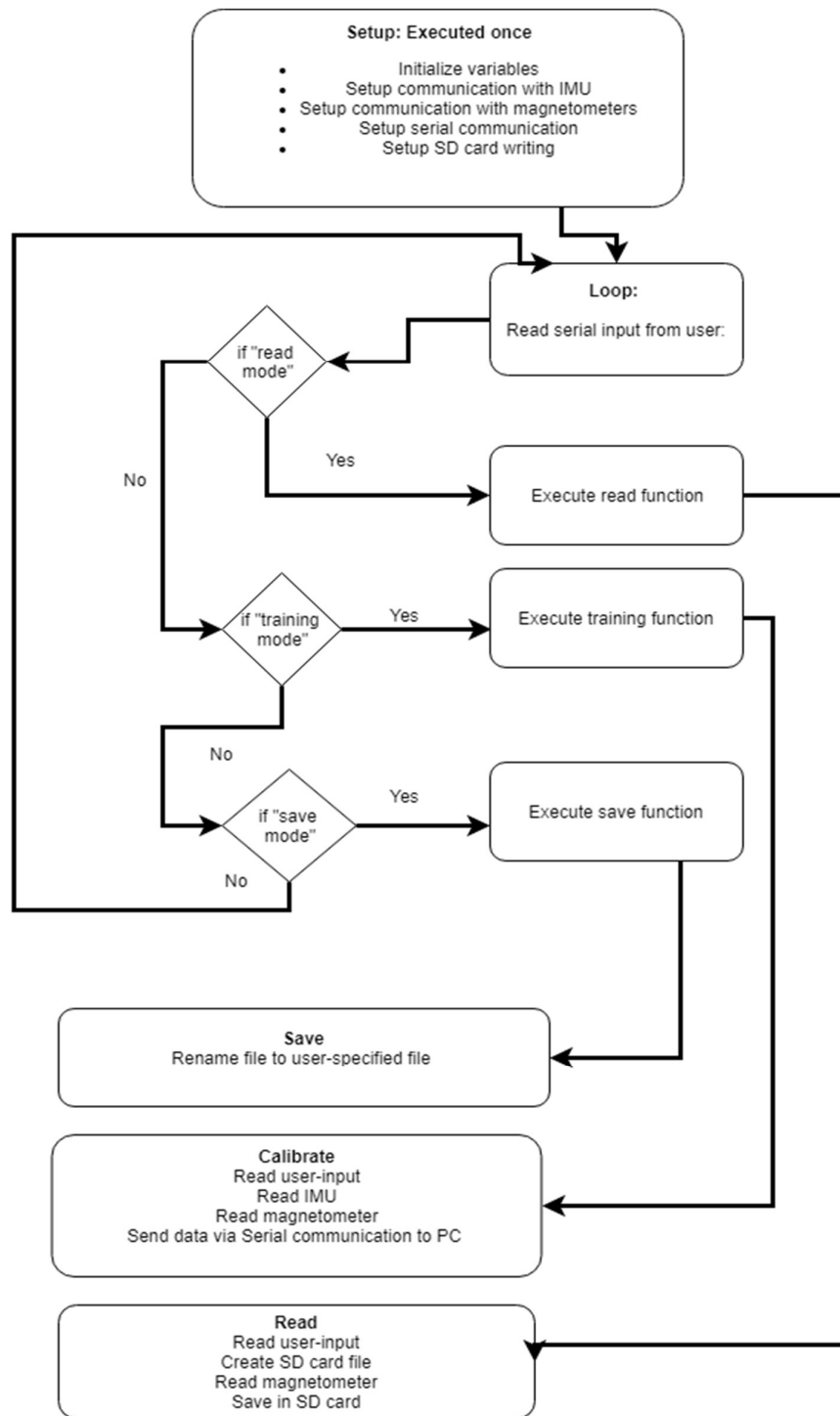


Figure 19: Microcontroller code flow diagram

3.4.2 Sensor libraries

Two sensor libraries were used. Both sensors communicated with the microcontroller through the I²C protocol. A sensor library for the IMU (BNO080) was provided by Sparkfun under the MIT open source license and is available on GitHub ('github.com', no date; 'www.sparkfun.com', no date; 'MIT @ opensource.org', no date). The library has two functions. Firstly, to establish communication and select the appropriate mode of the sensor. Secondly, to collect data from the sensor.

The IMU is set up by initializing a class, defined in the library. The class has methods to set up communication, select different modes, and requests the sensor for specific data.

The magnetometer did not have a library for the Arduino available. The sample code was provided for the magnetometer by the manufacturer (PNI Corporation) but it was not compatible with the Arduino IDE programming language. A new library was written for the Arduino IDE, following the same structure as the sample code provided by the manufacturer. The functions written for the magnetometer are an initialize and read function.

The initialize function sets up communication and selects the appropriate mode of the sensor. The magnetometer's cycle count, sample rate, max data rate and gain can be adjusted with the initialize function. The read function requests the sensor for the data.

3.4.3 GUI and data-capturing

Kivy is a Python library to create cross-platform applications. Kivy is a useful module to create GUIs because one can separate the program logic from the layout. The layout of the GUI is defined in a Kivy text script, executed in Python. The logic was written in Python.

Figure 20 shows the four screens that are selected with tabs when operating the device. The first screen is to connect the device to a COM of the PC. The second screen is the training screen. The third screen is where the user test if the training is sufficient. Lastly, the fourth screen is to put the device into read mode.

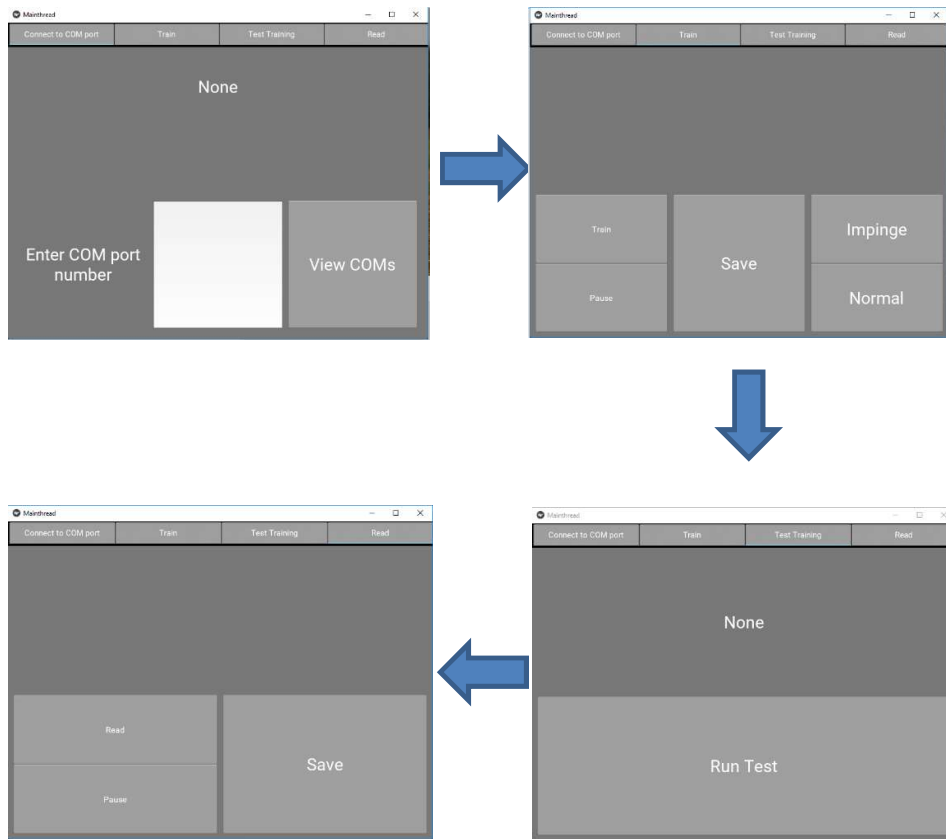


Figure 20: GUI tabs from left to right, top to bottom. Connect, training, test training and reading tabs

The layout is defined in .kv file. The application is relatively simple and didn't require a complex structure. Each screen in the application was associated with a specific class. Each button on a screen was associated with a method in that class.

The link between the GUI and the Python logic is the methods. Each method, defined in the .kv file, has a corresponding method in the Python script that is executed once that method is selected through a button on the application.

Figure 21 states the three classes with the methods in each class.

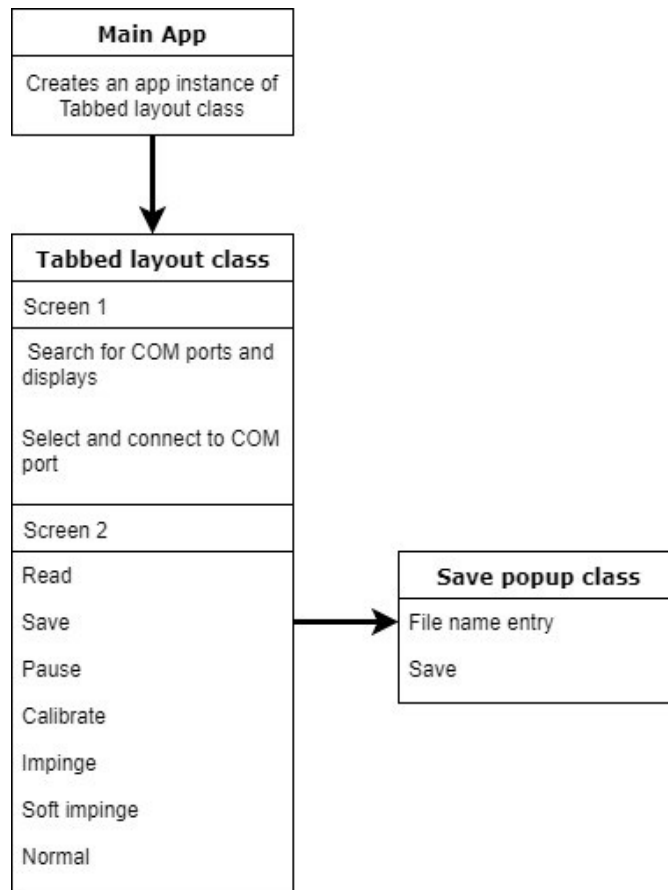


Figure 21: Kivy logic

3.4.4 Python post-processing code

This section explains the process of receiving the CSV file from the SD card to displaying the results. The process is illustrated in figure 22 and explained below.

The first step was locating and loading the CSV file into a database. The database used was Python's Pandas module (McKinney, 2010). This allowed for easy and fast data querying and manipulation. The training and testing data were calibrated, following the numerical operation explained in section 2. The numerical operations were performed using Python's Numpy module (Travis, 2006).

The calibrated training data was then used to train the machine learning model. The machine learning model was fed the calibrated testing data to predict the impingement instances. The instances are displayed in a plot consisting of a

change of impingement against time. Matplotlib module was used for the plotting requirements (Hunter, 2007).

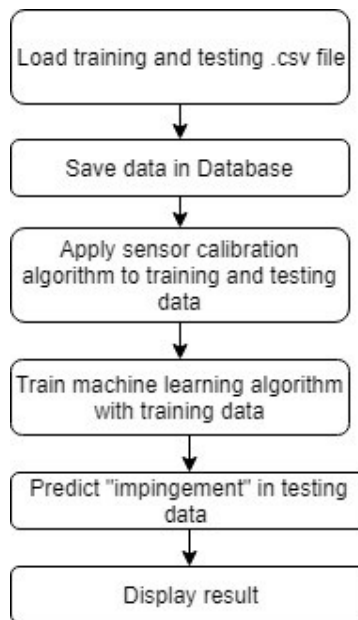


Figure 22: Post-processing data flow

3.5 Machine learning

This section discusses the machine learning algorithm implementation and the logic applied in selecting the specific algorithms.

3.5.1 Algorithm selection

The problem at hand is not a common machine learning problem. Traditionally the underlying data cannot be changed to suit the machine learning algorithm, apart from pre-processing. In this problem, the underlying data can be changed by changing the training process (physical movements) or moving the magnets to more appropriate locations. The changes to the training can affect two aspects of the training data: the quantity and the quality of data.

The quantity of data in training can be changed by simply extending the training period. The quality of the data can be changed through many variables. The most important of which is minimizing mislabelled data. The device relies on a user to label the data. The effect of this is that some errors can occur when the data is mislabelled.

These two changes have a combined effect on the data. If there is enough data but the quality is low, the accuracy will suffer, and vice versa. In order to exploit the fact that the data can be changed entirely to best fit a particular algorithm, one needs to apply some machine learning knowledge of algorithms to best choose an appropriate algorithm.

Intuitively a K-nearest neighbours (k-NN) or support vector machine algorithm will probably work best. The reason for this is from a technical stand-point the project is to “recognize” a magnetic signal as a unique position of permanent magnet’s magnetic field. The magnet moves relative to the magnetometers. Another way to look the problem is to imagine the magnet is stationary and the magnetometer “maps” the magnetic field around the magnet. Each point in space is associated with a magnetic vector in three-dimensional space. The magnetic vector must then be linked to a position of the hip. The position can be thought of as three-dimensional sub-spaces in the larger three-dimensional space.

The support vector machine functions by sets up a border between the ‘normal’ and ‘point of interest’ position. The k-NN algorithm is instance based and determines the class of an instance based on its neighbours. Both algorithms suite the problem. The researcher decided to focus on k-NN because designing the calibration procedure would be more intuitive with k-NN than a support vector machine.

3.5.2 Model implementation

This section discusses the machine learning algorithms used. Two different models were used in the project. The first was to evaluate the technique and establish if the signal from the magnets correlates with the anatomical angles of the hip. Secondly, the complete model used to predict a specific position is discussed.

Both models were tested separately in section 4. The first model uses a k-NN regression algorithm. The reason for using a regression algorithm is to establish an accuracy for the prediction of anatomical angles. The second model is a k-NN classification model. This model is used in the final device. Both models use the same underlying algorithm namely: k-NN. There are however slight differences in the prediction of the results for both.

The regression model is discussed first. The data from the magnetometer is first calibrated using the process described in section 2.2.2. The data has two categories. The features (X) and the labels (y). The features for the machine learning model was the calibrated magnetometer data and the labels are the angles measured by the Vicon. Each feature in X is paired with a corresponding angle in y. This was done by interpolating the Vicon data to time with the magnetometer data.

The data is shuffled and split into 80 % training data and 20 % testing data. The training features are scaled using Scikit-Learn's StandardScaler (Pedregosa *et al.*, 2011) function. The function centers the data at the mean and divides it by the standard deviation of the feature. This ensures that one feature does not dominate.

Next, the k-NN model is trained with the data. The model parameters were left to default except for the "weights" parameter. All the parameters were as follows:

Table 4: Regression model parameters

PARAMETER	VALUE
N_NEIGHBOURS	5
WEIGHTS	Distance
ALGORITHM	Auto
LEAF_SIZE	30
P	2
METRIC	Minkowski
METRIC_PARAMS	None
N_JOBS	1

The "distance" weight was selected to weight points closer to the label more than those further from the label. The weights applied is inversely proportional to the distance to the points. The other parameters weren't optimized because it did not fit into the goal of the study described in section 4. The difference between the results was negligible. The unoptimized results were inside the desired accuracy of 5°. The model then receives the testing features to make a prediction. The predicted values are compared with the actual values to calculate an error.

The classification model uses different training and testing data for the regression model. The calibration also changes to better handle the influence of the earth's magnetic field. Additional pre-processing steps were implemented in the classification model as well as an additional magnetometer positioned on the opposite hip. The additional pre-processing algorithm is described mathematically in section 2. The algorithm orientates all the magnetometers on the same coordinate system. The magnetometer with the least amount of influence from the permanent magnet measures predominantly the earth's magnetic field. Depending on the orientation of the magnet, the magnitude of the earth's

magnetic field is 10 times larger than the signal of the magnet. The magnetometer data from this magnetometer is subtracted from the other two magnetometers to get to isolate the signal from the permanent magnet.

In the classification model, the training data and testing data were collected separately. The training and testing data are scaled separately thereafter with the same scaling technique used in the regression model. The k-NN model was trained and predicted a “percentage nearest neighbours that are a point of interest”. The k-NN classification model parameters are as follows:

Table 5: Classification model parameters

Parameter	Value
N_neighbours	$N/2$ where N is the number of points of interest in the training set
Weights	Distance
Algorithm	Auto
Leaf_size	30
P	2
Metric	Minkowski
Metric_params	None
N_jobs	1

Only the weights and n_neighbours were changed from the default. The other parameters were left on default because it would not affect the results significantly and has more of an influence on the computational time.

For the weighting, distance was selected. This weights the neighbours closer to the instance higher than those far away from the instance. The weighting is calculated as an inverse of the distance from the instance. Weighting the nearest neighbours by distance makes intuitive sense and produced the best results.

It is known that k-NN does not work well on unbalanced datasets. The researcher tried to overcome this problem by adapting the training procedure and collecting the same amount of data points for each class. It is, however, difficult to get as many data points in the “point of interest” class as in the “normal” class. An oversampling algorithm was implemented to overcome this problem. Synthetic Minority Oversampling Technique (SMOTE) was implemented (Lemaître, Nogueira and Aridas, 2017). SMOTE generates new samples by interpolating the

undersampled data with a k-NN algorithm. The most important algorithm parameter is the amount of the nearest neighbours. The amount selected was $N/2$, where N is the number of undersampled samples.

Another challenge with the implementation of the k-NN algorithm is the ability to deal with high dimensionality data. The reason for this is because the higher the vector space, the less significant the distance measurement is. The data used has a dimension of 6 because there are six features. The features consist of X, Y and Z axis of the two sensors. The problem was split into two models, one for each sensor. This reduces the problem to two, three-dimensional problems.

The two models were trained simultaneously, and each model and predicted the output separately. The outputs from each model are weighted inversely to the total signal strength. This has two advantages. It reduces the dimension of the problem and from a physical sense, the magnetometer closest to the magnet has a higher influence on the output.

3.6 System synthesis

The device went through several iterations of improvements. This section discusses the most significant improvements made throughout the development of the device in order for the sub-systems to function as a whole system. The interaction between the software and the hardware is already explained in section 3.2, 3.3 and 3.4. The section discusses the aspects that were not discussed in those sections.

3.6.1 Hardware placement

The magnet is placed on the IT-band (iliotibial-band), three-quarters of the way up on the femur, measured from the knee. The placement was selected because it is the most stable (less soft tissue artifacts) section on the upper leg that is near the pelvis. Three magnetometer sensors were used. The first one is placed on the ASIS and the second on the top part of the iliac crest. The third is placed on the opposite hips ASIS. This placement tries to minimize soft tissue artifacts.

Evaluating these placements against the requirements for the device resulted in the following conclusion. Requirement 1 (robustness) is achieved by the placement because the magnets itself is robust and the sensors are small enough to be housed in a strong capsule. Requirement 2 (accuracy) is the most affected by the placement of the magnet and sensors. As previously mentioned, the placement minimizes soft tissue artifacts while maintaining a close enough distance between the sensors and magnets. The placement was modelled after the placement of the Vicon (Vicon Motion Systems Ltd., Oxford, UK) motion tracking system marker placement used in the pilot study. Requirement 3 (user-

friendly in use) is met because the placement does not impact the user's ability to perform movements.

The placement of the central unit and battery do not impact the function of the device. The placement of these two can thus be made depending on the activity to least impact the user.

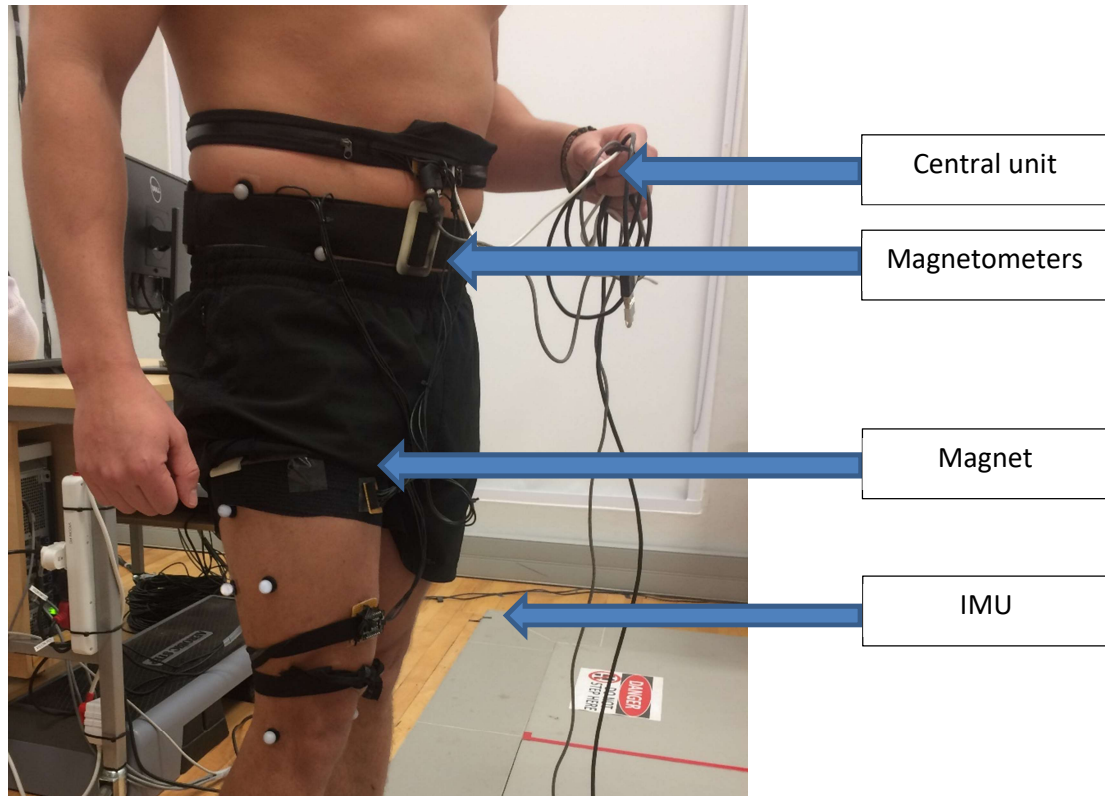


Figure 23: Hardware placement

3.6.2 Magnet selection

The strength and type of all the magnets tested was N38 neodymium magnet. The reason for only testing one type and strength of the magnet is it was the strongest magnets readily available. Selecting the magnets shape and size were done iteratively after estimating the best shape by applying the conclusions reached in section 2.

In section 2, it was discussed that the magnetic field of a dipole is twice the strength on the axis of the dipole compared to the other two perpendicular axes in three dimensions. Furthermore, the strength of a magnetic field is directly proportional to the volume of the magnet for the same magnetization.

These insights were applied to selecting a magnet in the following manner: Firstly, it would be better to align the magnets axis towards the sensor, as this would achieve a stronger magnetic field for the same magnet. Secondly, the shape of the magnet can be altered by placing multiple magnets on top of each other to create a new magnet field. The new magnetic field would be directly proportional to the change in volume.

The magnet shapes available were discs (magnetized through the thickness), rectangles (magnetized through the thickness) and cylinders (magnetized through the length). The cylindrical shape magnets were used for the primary benefit of aligning the axis magnetization axis towards the sensors.

4 Pilot study

The pilot study was designed in a two-step process. The initial rounds of testing aimed to assess the device against the requirements set out in section 1. The overall functionality of the device was assessed and the feasibility of determining human kinematics through permanent magnet tracking.

After the first round, minor improvements to the device were made and tested in the second round of testing. The goal of the second-round testing was to validate the accuracy of the device and

refine the machine learning algorithm.

Both rounds of testing involved comparing the device against a gold standard optical motion tracking system. The system used was the Vicon Vantage (Vicon Motion Systems Ltd., Oxford, UK) motion capture system. The system consisted of 10 Vicon Vantage 5V cameras. The system is known for its accuracy and is frequently used to evaluate IMU-based motion tracking systems (López-Nava and Muñoz-Meléndez, 2016). Both studies were conducted at the Neuromechanics lab in Stellenbosch. The staff at the Neuromechanics unit processed the data from the Vicon and supplied the researcher with the relative hip angles using the Vicon's lower body plug-in gait model with a timestamp (Kadaba, Ramakrishnan and Wootten, 1990).

4.1 Participant inclusion/exclusion criteria:

Five healthy individuals were recruited for the study. The participants must not have suffered any hip impingement syndrome symptoms. The symptoms include tightness or discomfort in the hip, pain in the hip during or after activity. The participants should have been able to complete all the prescribed movements correctly. Ethical approval to conduct the study was achieved (see appendix A).

4.2 Pilot study 1

4.2.1 Protocol

Four participants took part in the initial pilot study, each participant was tested separately. Firstly, the optical motion markers were attached to the participant. A modified lower-body marker set was used that included 14 markers. The reason for modifying the standard marker set, recommended by Vicon, was because some of the pelvis markers were obscured during the calibration movement task. The markers were placed in the following locations: medial and lateral right ankle, right tibia, medial and lateral right knee, three markers on the thigh, left and right posterior superior iliac, left and right anterior superior iliac and the left and

right superior iliac crest. Next, the device was attached to the participant. Sports tape were used to attach both the device and markers.

The participants then completed the series of movement tasks listed in table 6. Each movement task was completed five times. The device and the Vicon was time synced with a high voltage signal through an auxiliary cable. The device read in a high signal of 5V when the Vicon started recording. The device was specifically modified to accommodate this cable. After each movement, the Vicon data was saved and stored. The whole sequence of movements was then be repeated three times. The movement tasks consisted of squatting, lunging and training per round. The squatting and lunging movements were completed five times and the training once per round.

Table 6: Movement tasks

MOVEMENT	MOVEMENT DESCRIPTION	TIMES PER ROUND
TRAINING	The participants lie on their back while performing the training procedure. The participants were asked to identify a point at around 70-degree flexion, 0 degrees internal/external rotation and 0-degree abduction/adduction which they can comfortably achieve lying down, squatting and lunging. This point will be referred to as the point of interest. Five right hip flexion and extension movements were made, each time moving past the point of interest. Next five adduction/abduction movements were made, with his/her leg being held subjectively at the point of interest in flexion/extension and internal/external rotation. Thereafter five internal and external rotations were performed moving past the point of interest in the internal/ external rotation. The participant tried to hold flexion/extension and adduction/abduction at the point of interest. Lastly, the participant was asked to hold the hip in the calibration position for 30 seconds	1
SQUAT	The participant performed five squats, focusing on moving through the point of interest	5
RIGHT FOOT FORWARD LUNGE	The participant performed five right foot forward lunges, focusing on moving through the point of interest.	5

4.2.2 Results: Pilot study 1

The first part of the results analysis consists of the evaluation of the requirements of the device.

- **Robustness:** The device in its current form is not robust. The device can, however, be improved by adding a protective cover to the sensors. This was not done in the pilot study phase to make troubleshooting easier.
- **User-friendly in use:** All the participant reported the device was convertible and did not inhibit any of the prescribed movements.
- **Stand-alone device:** This requirement was not met in the first pilot study because the Vicon data was used for the training of the system. This requirement is addressed in the second pilot study.
- **Accuracy:** The accuracy was evaluated but only to check for feasibility. The accuracy and feasibility are discussed below.

The second objective of the study was to establish if the device is capable of measuring anatomical angles of the hip. The procedure to establish if this is the case were as follows: The data from the magnetometers and the Vicon was time synced by interpolating the Vicon data with the magnetometer data. The Vicon sampled at 200 Hz and the magnetometers sampled at 150 Hz.

The dataset consists of six features (X). The six features are two magnetometer's x, y and z-axis magnetic flux density signal. The labels (y) are the three hip angles that were received from the Vicon. The whole feature set was calibrated for magnetometer errors with the process explained in section 2. The dataset was then shuffled and split into 80 % training set and 20 % test set. The training and testing set was then scaled separately to avoid information leaking from the training to the testing set. The kNN regression model was trained on the training set and tested on the testing set.

The difference in angle for each prediction from the model was calculated for the testing set. The whole process is summarised in figure 24.

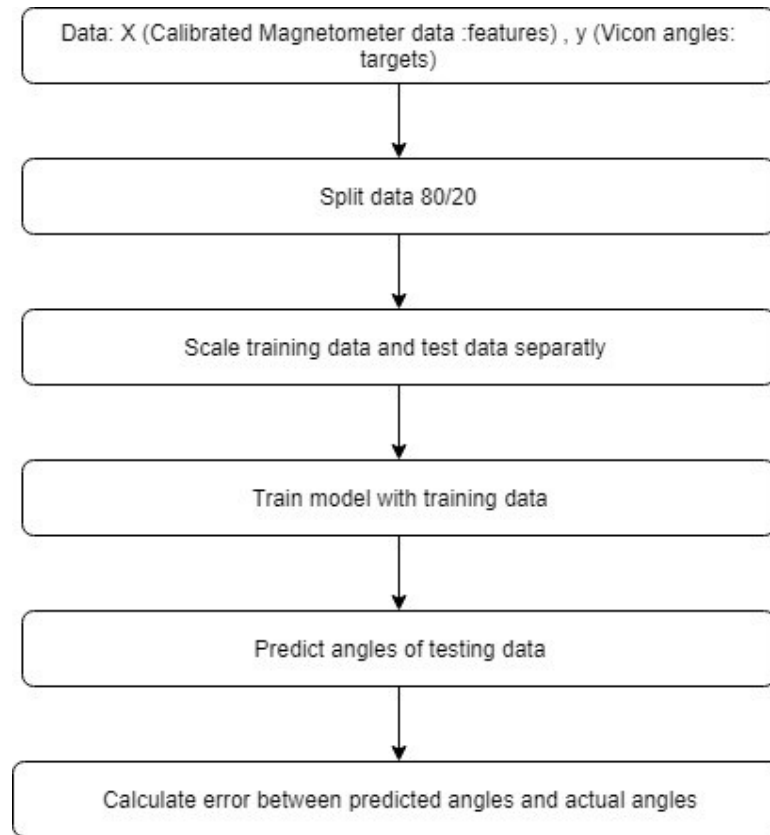


Figure 24: Pilot study 1 machine learning pipeline

The machine learning pipeline explained above was repeated for multiple datasets, each time calculating the average difference in angle and standard deviation of the difference in angle between the point of interest and the predicted angle. Each participant's data set was tested separately. The difference in angle calculated for each participant was placed in an array. The average difference in angle and the standard deviation of the difference in angle was calculated for each participant and plotted in figure 26, 27 and 28. The difference in the angle calculation process is displayed in figure 25.

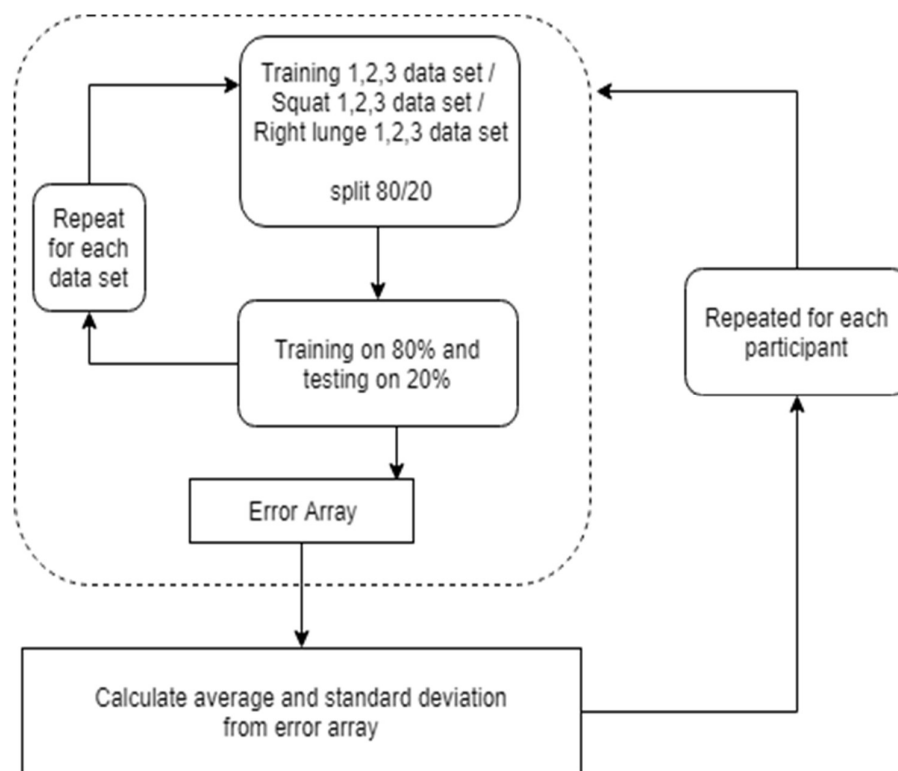


Figure 25: Difference in angle (error) calculation for pilot study 1

As visually explained in figure 25, the average and standard deviation were only taken once for each participant. The difference in angle (error) array consisted of nine tests per participant. For example: The training dataset for round 1 and participant 1 was tested. Next, the training dataset of round 2 of participant 1 was tested. Until all the dataset of the participant was tested. The whole sequence was repeated for each of the four participants.

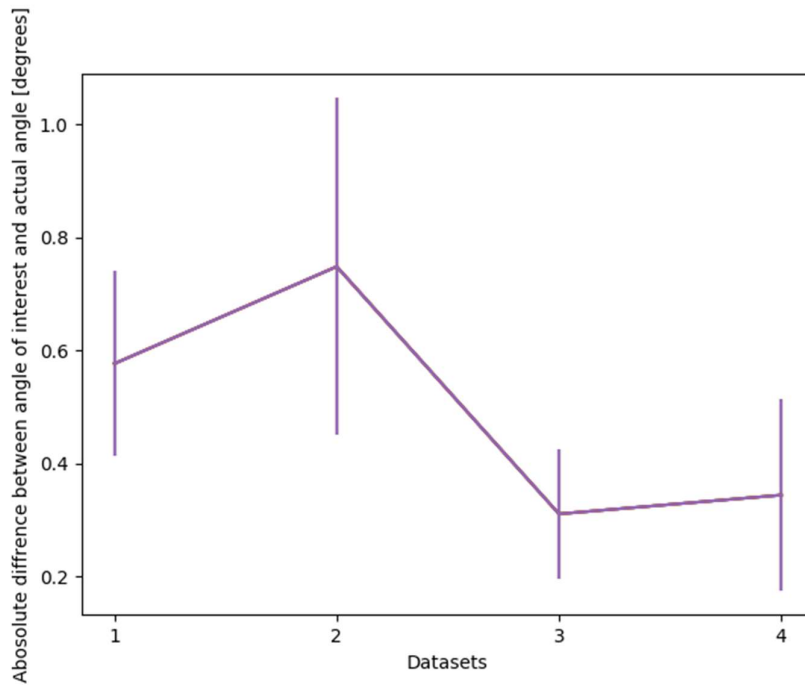


Figure 26: Average error and standard deviation in flexion/extension

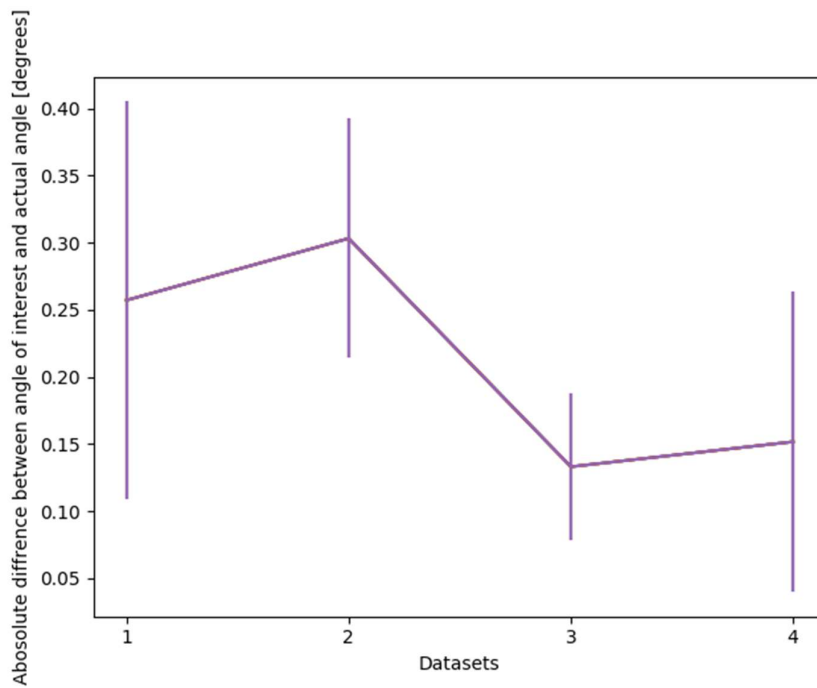


Figure 27: Average error and standard deviation in ab/adduction

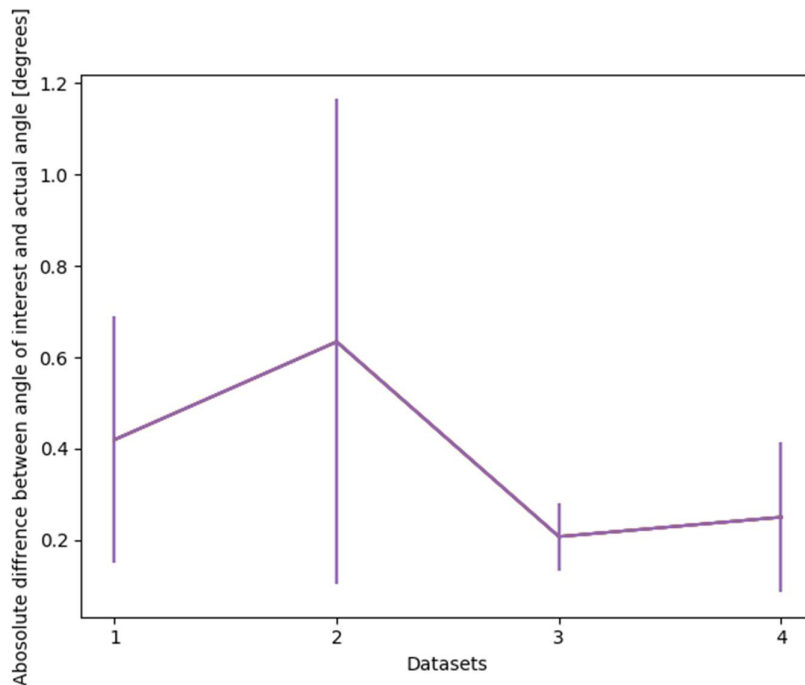


Figure 28: Average error and standad deviation in internal/ external rotation

4.2.3 Discussion: Pilot study 1

In figure 26, 27 and 28 the results; average and standard deviation for each participant, is displayed. Participant two had the weakest results. This was likely due to more soft tissue artifacts although no evidence can be provided for this. The accuracy was sufficient and indicates that the method is feasible for predicting hip angles. All the accuracy is out of sample accuracy, the algorithm is thus not overtrained.

The objective of the study was achieved. The hyper-parameters weren't tuned for the optimal result because the primary objective was already achieved, and it would not aid in further work. The hyper-parameters would need to be retuned in the second pilot study, it would thus not make sense to achieve an optimal result in the first pilot study only to retune the parameters in the second pilot study. The algorithm refinement was addressed in the second pilot study. The main shortcoming identified in the first study was the greater than anticipated influence the earth's magnetic field would have on the device. This was also addressed in the second pilot study.

4.3 Pilot study 2

4.3.1 Protocol

Only one participant took part in the second pilot study. Firstly, the optical motion markers attached to the participant. Next the device, but without the magnet, was attached to the participant. The participant was asked to turn 360 ° and do arbitrary movements for 30 seconds. This is an additional calibration task that was not performed in the first study. The magnets were only attached after this movement was completed. The participant then completed the series of movements. Each movement task (excluding the calibration) was be completed five times. The whole sequence of movements was then be repeated three times.

All the movement task stays the same except for a slight addition prior to the training. An additional squat was also performed per round in the second pilot study. The reason for this was to test if the earth's magnetic field would have an influence on the device.

4.3.2 Objectives

The first objective of the second pilot study was to improve the shortcomings that were identified in the initial pilot study in terms of the requirements. The algorithm was also refined to achieve the best output in terms of accuracy. The second objective was to determine the accuracy of the device against Vicon optical motion tracker.

4.3.3 Results: Pilot study 2

After the evaluation of the results in pilot study 1, two hardware changes were made. The first was removing the IMU because it didn't add any value to the pre-processing. The IMU's intended use was to eliminate the data that was incorrectly labeled by the user. The IMU was too inaccurate to make a noticeable difference and deemed unnecessary as it didn't add any meaningful value.

Secondly, another magnetometer was added to assist in noise minimization of the earth's magnetic field. All three the magnetometers were aligned to a signal axis system by implementing the algorithm explained in section 2. The third magnetometer was placed on the opposite ASIS than the other magnetometer. The third magnetometers data was then subtracted from the other two magnetometers to remove the bias of the earth's magnetic field.

The results were evaluated in a similar manner to the structure of a confusion matrix mentioned in section 2 of the report. The classification task is a soft classification task and using strictly a confusion matrix will give a misrepresentation of the results. The results were evaluated by first considering

the error in positive predictions. This encapsulates the false positive and true positive readings from the confusion matrix as marked with the red circle in table 5.

Table 7: False positive section of the confusion matrix

		ACTUAL	
		Positive	Negative
PREDICTED	Positive	True positive	False positive
	Negative	False negative	True negative

For each participant, the following test was run. The training data was used to train the machine learning algorithm. The output was a percentage nearest neighbours that were nearest to a point of interest. That is for the squat of round 1, 2 and 3, the right lunge of round 1, 2 and 3, the squat at a different orientation of round 1,2 and 3 and the training of round 2 and 3. The process was repeated for the training of round 2 and 3.

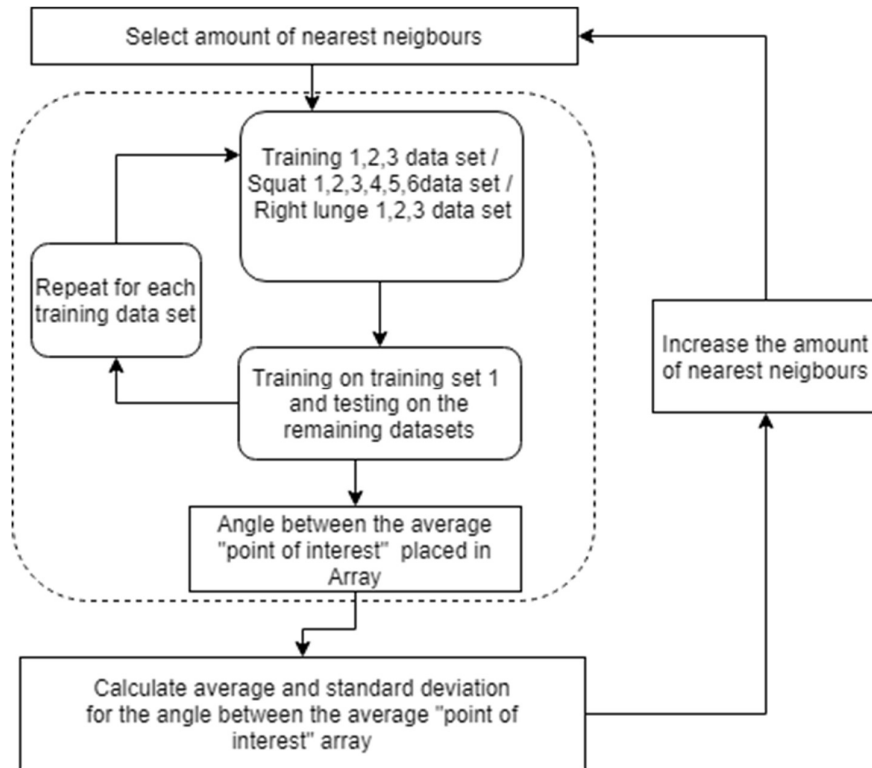


Figure 29: Difference in angle calculation for pilot study 2

The difference in angle between the average point of interest and the actual angle at that time instance was calculated each time the algorithm had an output larger than 1%. The difference in angle was calculated in degrees of the marked point of interest in training. All the differences were stored in a list. The average and standard deviation of the list of differences were only taken once and displayed in figure 30, 31 and 32.

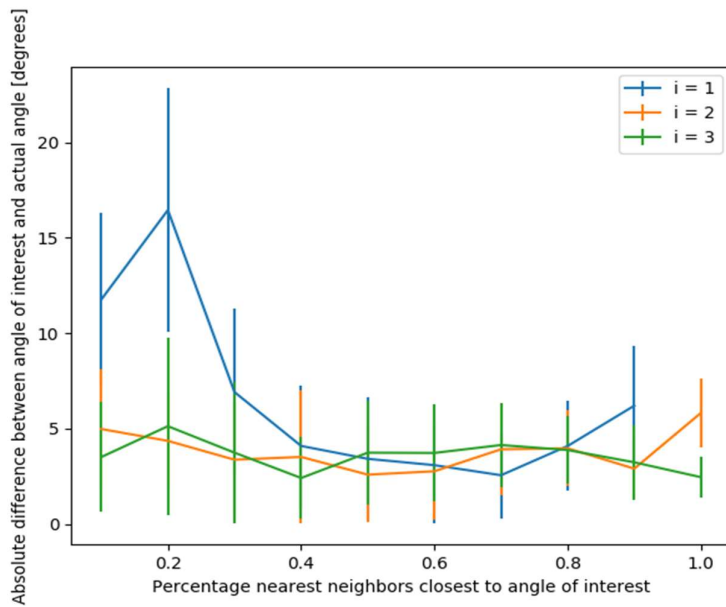


Figure 30: Absolute difference in the angle between the average point of interest for the percentage nearest neighbours closest to the point of interest for different values of I in flexion / extension

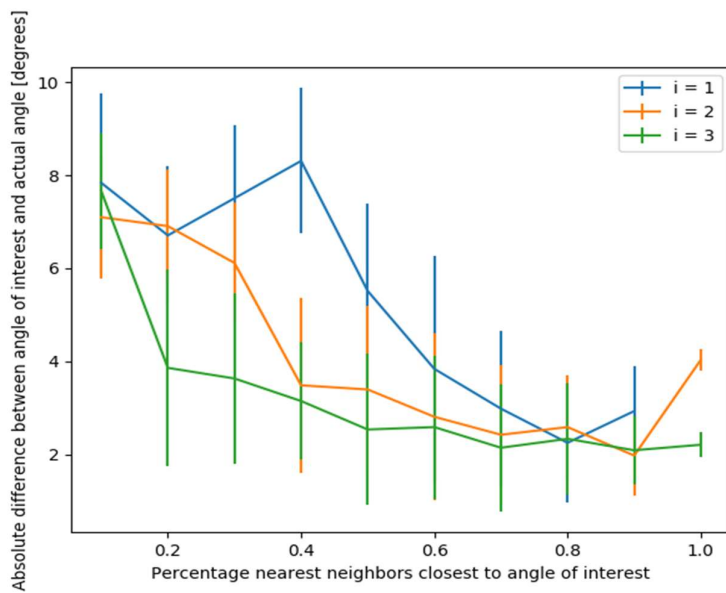


Figure 31: Absolute difference in the angle between the average point of interest for the percentage nearest neighbours closest to the point of interest for different values of I in the abduction/adduction

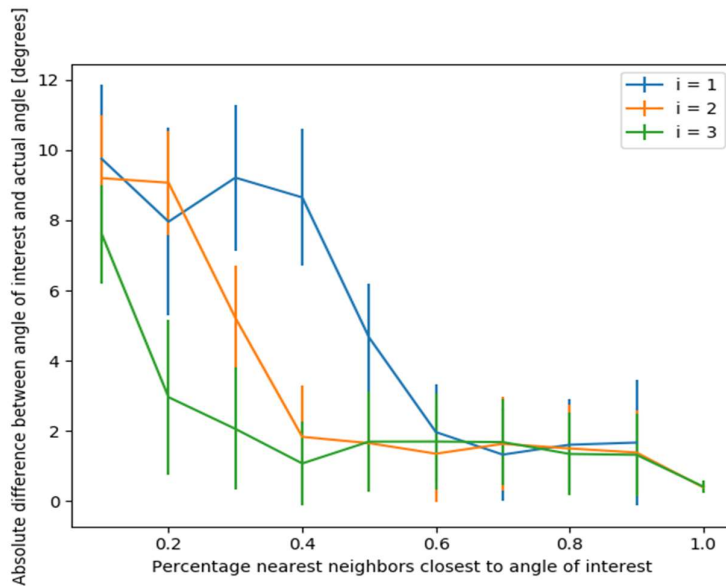


Figure 32: Absolute difference in the angle between the average point of interest for the percentage nearest neighbours closest to the point of interest for different values of i in the internal/external rotation

The accuracy above in figure 30, 31 and 32 gives an indication of the accuracy of a positive prediction and the sensitivity. Measuring the false negatives in a soft classification task is necessary to estimate the specificity. Figure 32 indicates the false negatives instances for the device. This ties into the confusion matrix as indicated in table 7 and marked with the red circle.

Table 8: Confusion matrix being addressed in the following section

		ACTUAL	
		Positive	Negative
PREDICTED	Positive	True positive	False positive
	Negative	False negative	True negative

The false negatives were calculated as follows: Each time the individual reached a hip position with a specific tolerance in X, Y, and Z, it was marked as a “point of

interest". The tolerance selected was input as a variable in degrees. This transforms the problem into a hard classification task. It is necessary to transform the problem into a hard classification task to count the false negative instances.

All the combinations of training and testing data were run to test for instances where the hip reached the selected tolerance zone but did not produce an output of larger than 1 %. This was then labeled as a false negative. The process is displayed in figure 33.

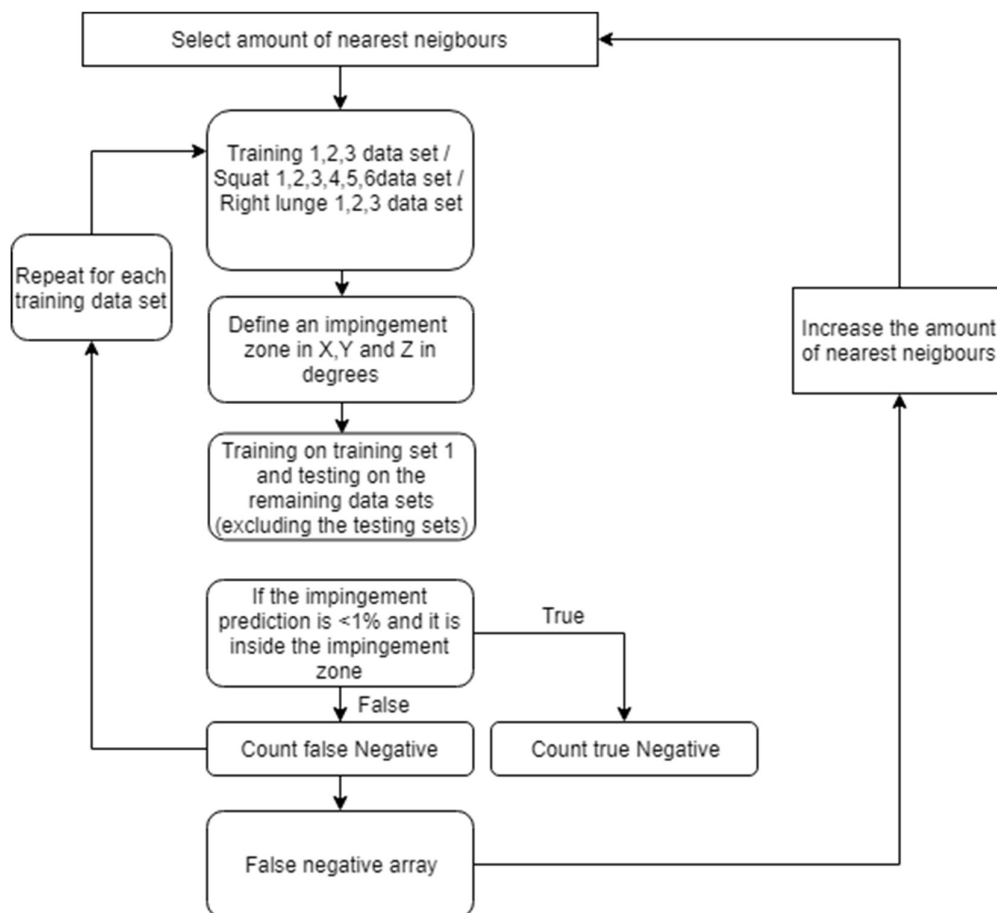


Figure 33: Calculating the false negatives flow diagram

As indicated in figure 33, the process was repeated for N/i (where $i = [1,2,3,4,5,6]$) amount of nearest neighbours and for different angle tolerance zones in degrees. Figure 34 shows how the tolerance zone was increased in one dimension. The step was repeated for all dimensions.

The different lines represent a different amount of neighbours for kNN. The legend displays i , where the amount of nearest neighbours are N/i , where N is the number of training instances that has is in the “point of interest” class.

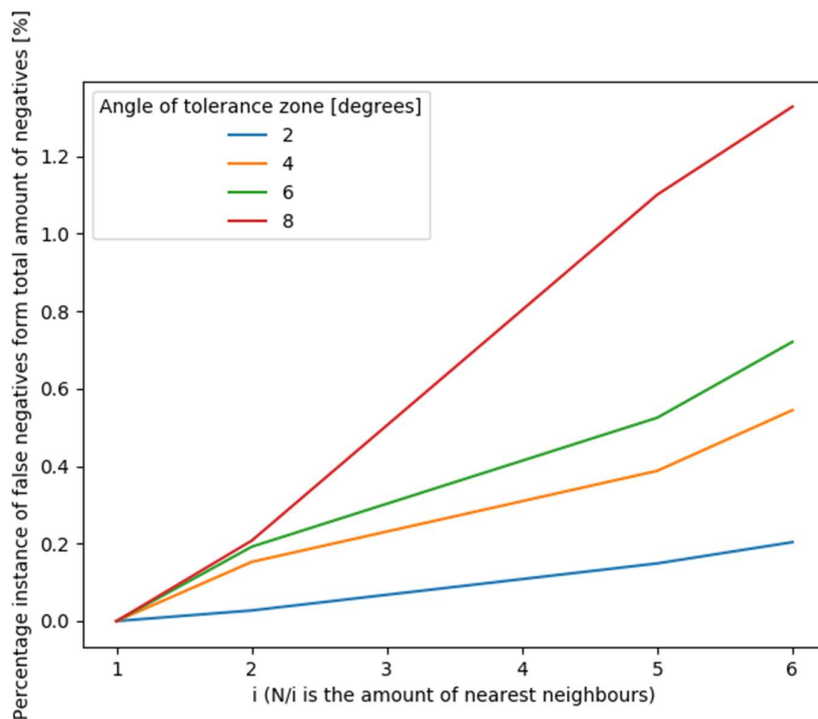


Figure 34: False negative instances for k in k-nn for different tolerance zones

4.3.4 Discussion: Pilot study 2

In section 3.5 it was already stated that the amount of nearest neighbours selected was $N/2$. It was important in the selection of the nearest neighbours to achieve a sufficient trade-off between sensitivity and specificity. The researcher decided that an $N/2$ achieves the appropriate trade-off.

Figure 30 displays the absolute angle between the point of interest and the output percentage. The output stays constant for all outputs. Figure 30 has to be considered in the context of figure 31 and 32. If the device outputs a percentage of 30%, it is likely that the hip’s position is in the range of 5 degrees in flexion from the point of interest but only within 5 degrees in ab/adduction and 6 degrees in internal/external rotation. The combination of the three degrees must be taken

into account when considering the output. From figure 30 to 32 it can be seen that the device is ab/adduction and internal/external rotation sensitive. This result is preferable in the context of hip impingement because hip impingement is dependent on the combination of the three angles, and not dependent only on one. The standard deviation of the angles in figure 30, 31 and 32 is large but if one considers soft tissue artifacts it is acceptable in the context.

Figure 34 gives an indication of the false negatives. It is expected that for i equal to 1, there would be no false negatives because there would always be the nearest neighbour in the “point of interest” class. As i increases so does the false negatives. This is expected as the system becomes more specific. As the angle of tolerance zone increases, so does the amount of false negatives. There is a clear divergence between the 4- and 6-degree tolerance zone and the 8-degree tolerance zone for i equal to 2. This weighed in the trade-off in sensitivity and specificity in the selection of the amount of nearest neighbours. The main shortcoming identified with the procedure is that no noise from the earth’s magnetic field is introduced in training. The machine learning algorithm was chosen with this shortcoming taken into consideration. The earth’s magnetic field noise was rather compensated for by measuring it independently.

The results are acceptable when compared to the current method of determining hip impingement in patients. Currently used is a software simulation package (Articulis, Clinical Graphics) that simulates the movement of the hip in three dimensions from a CT-scan to a maximum error of 5.4° (Röling *et al.*, 2015). The device demonstrated a maximum error in the same range.

Additionally, when the device is compared to Xsens’s commercial solution, its performance is comparable. The commercial IMU solution achieved a maximum root mean square error of 10.3° in flexion of the hip joint (Chepers, Giuberti and Bellusci, 2018). The error of the commercial IMU is, however, compared with an OpenSim (Delp *et al.*, 2007) simulation which models the movement of the bones. Previously mentioned Cockcroft (2015) achieved a maximum mean error of 6.7° internal/ external rotation but with large variability in the results. When assessing the device against the other requirements set out in section 1.3, the device performed well. The device will be able to operate outside a lab environment. The device was also comfortable for all the participant and did not interfere with the movements performed. The device can also be protected with an enclosure to be made more robust. It can also be speculated, with a high degree of confidence, that the device would be less impacted by impact sports than an IMU-based unit. The reason for this is due to nature of the technology not relying on inertia measurement but rather determining positions.

Furthermore, another shortcoming was identified in the pilot study design. In section 2, it was stated that a magnetic field depreciates cubically. This causes the

system to become more sensitive, the closer the magnet is to the magnetometer. The pilot study did not test end ROM but rather mid-ROM of the participants. The participants thus moved through the points of interest. This resulted in a system that would not be as sensitive as the intended use case of the final system. The sensitivity would be expected to be greater if only an end ROM is measured.

The same argument can be applied for the specificity, as most of the false negatives occurred due to a low signal strength because the magnets were far away from the magnetometers. A second shortcoming identified in the pilot studies was the lack of motion in ab/adduction and internal/external rotation. This affected the results because the accuracy in ab/adduction and internal/external rotation direction looked better than in flexion /extension because the ROM in the ab/adduction and internal/external rotation was limited. The average errors reported would thus not be that heavily affected by a wrong prediction as in the case of flexion/extension (see appendix B).

5 Conclusion

The project was a success because it was sufficiently proven that the prototype can meet all the requirements in the final device. Multiple technologies namely, machine learning, magnetics and embedded systems, were brought together to create a novel position tracking device for the hip. Although the device still needs some work to be used in a clinical setting, a good basis was developed that can be improved upon.

5.1 Device design

All the design requirements were considered in the design process with a key focus placed on accuracy. The final device consisted of an Adafruit Feather Adalogger microcontroller and data storage device connected to three PNI's RM3100 magnetometers. A lithium-ion battery supplied the power.

The device functioned in a three-step process. Firstly, the device was trained for the specific position it needed to detect. Thereafter the device detected the trained position. The data was downloaded and post-processed to detect the instances.

A GUI was designed in Kivy together with Python to facilitate easy setup. Scikit-learn's KNN algorithm with $N/2$ nearest neighbours was selected as the algorithm for position detection. Where N is the amount of training "points of interest" instances.

5.2 Outcomes

The pilot studies set out to assess the requirements. The final device, tested in pilot study 2, is discussed with regards to the requirements.

Following the main objective, the requirements of the device are:

1. **Robustness:** The sensors can be easily placed in a robust capsule to protect it from the elements without impacting the users. The sensor can also be further shrunk down because there is a lot of unused space on the bought in sensor breakout boards.
2. **Accuracy:** The accuracy of the device was within 5 ° for a high percentage nearest neighbours' output. False negatives were also acceptably low for $N/2$ nearest neighbours.
3. **User-friendly in use:** All the participants reported that the device didn't inhibit the movements that they completed. There is room for improvement to

better secure the sensors on the hip to avoid them from shifting after calibration, but it is a fault that can be easily rectified taping the sensors in place.

4. Stand-alone device: The device can be used outside of a lab environment. Only the calibration of the current device must be facilitated by a computer.

Shortcomings were also identified. The most significant of which was the influence of the earth's magnetic noise. An additional magnetometer was placed on the opposite hip to measure the earth's magnetic field independently was added to the device for testing in the second pilot study.

5.3 Future work

Future work would be to better quantify the drift accuracy of the device. Although it is theorized that there should not be drift as associated with IMU, it was not tested and can thus not be said with certainty.

On the hardware side of the project, the capsule and sensor mounting options can be addressed. On the software side, however, there is a lot of development opportunity available. A relatively simple machine learning algorithm was deployed in this project. Improvements can be made if a more complex algorithm is used in conjunction with an alternative training procedure to capture the earth's magnetic field data in the training algorithm. Being able to include the main source of noise (earth's magnetic field) in the training data will result in an improvement in accuracy.

Thereafter the device can be refined into a sleek, ready-to-use device to be used for its intended clinical application and progress the state of hip impingement research.

6 References

- Agricola, R. *et al.* (2013) 'Cam impingement causes osteoarthritis of the hip: a nationwide prospective cohort study (CHECK)', *Annals of the Rheumatic Diseases*, 72(6), pp. 918–923.
- Bedi, A. *et al.* (2008) 'The Management of Labral Tears and Femoroacetabular Impingement of the Hip in the Young, Active Patient', *Arthroscopy - Journal of Arthroscopic and Related Surgery*, 24(10), pp. 1135–1145.
- Besl, P. and McKay, N. (1992) 'A Method for Registration of 3-D Shapes', *IEEE Transactions on Pattern Analysis and Machine Intelligence*, pp. 239–256. doi: 10.1109/34.121791.
- Bianchi, A. and Oakley, I. (2015) 'MagnID : Tracking Multiple Magnetic Tokens', pp. 61–68.
- Blanchard, B. S. and Fabrycky, W. J. (2014) *Systems engineering and analysis*. Pearson.
- Chan, P. Y. and Ripin, Z. M. (2013) 'Development of Wearable Inertial Sensors for Measurement of Hand Arm Tremors'.
- Chen, K. *et al.* (2013) 'uTrack : 3D Input Using Two Magnetic Sensors', *Sensing*.
- Chen, P. *et al.* (2015) 'Real-Time Human Motion Capture Driven by a Wireless Sensor Network', *International Journal of Computer Games Technology*.
- Chepers, M., Giuberti, M. and Bellusci, G. (2018) 'Xsens MVN: Consistent Tracking of Human Motion Using Inertial Sensing'. doi: 10.13140/RG.2.2.22099.07205.
- Cockcroft, J., Muller, J. H. and Scheffer, C. (2014) 'A novel complimentary filter for tracking hip angles during cycling using wireless inertial sensors and dynamic acceleration estimation', *IEEE Sensors Journal*. IEEE, 14(8), pp. 2864–2871. doi: 10.1109/JSEN.2014.2318897.
- Cockcroft, S. J. (2015) *Novel motion capture methods for sports analysis : case studies of cycling and rugby goal kicking*.
- Delp, S. L. *et al.* (2007) 'OpenSim: Open-Source Software to Create and Analyze Dynamic Simulations of Movement', 54(11), pp. 1940–1950. doi: 10.1109/TBME.2007.901024.
- El-gohary, M. A. (2013) *Joint Angle Tracking with Inertial Sensors by*.

EM GeoSci — Electromagnetic Geophysics (no date). Available at: <https://em.geosci.xyz/index.html> (Accessed: 27 June 2018).

Fairley, J. *et al.* (2016) 'Management options for femoroacetabular impingement: a systematic review of symptom and structural outcomes', *Osteoarthritis and Cartilage*. Elsevier Ltd, 24(10), pp. 1682–1696. doi: 10.1016/j.joca.2016.04.014.

Feynman, R. P., Leighton, R. B. and Sands, M. L. (2010) *The Feynman lectures on physics*. Basic Books. Available at: <http://www.feynmanlectures.caltech.edu/>.

Forsmark, C. (2017) 'Investigation of magnetic sensors and hardware design of a sensor platform for human-computer interaction purposes Investigation of magnetic sensors and hardware design of a sensor platform for human-computer interaction purposes'.

Frank, J. M. *et al.* (2015) 'Prevalence of Femoroacetabular Impingement Imaging Findings in Asymptomatic Volunteers: A Systematic Review', *Arthroscopy : the journal of arthroscopic & related surgery : official publication of the Arthroscopy Association of North America and the International Arthroscopy Association*. Arthroscopy Association of North America, 31(6), pp. 1199–1204. doi: 10.1016/j.arthro.2014.11.042.

Freescale Semiconductor (2013) 'Xtrinsic MAG3110 Three-Axis , Digital Magnetometer', (MAG3110), pp. 1–30.

Géron, A. (2017) *Hands-On Machine Learning with Scikit-Learn*. O'Reilly. doi: 10.3389/fninf.2014.00014.

'github.com' (no date). Available at: https://github.com/sparkfun/SparkFun_BNO080_Arduino_Library/blob/master/LICENSE.md.

Griffin, D. R. *et al.* (2016) 'The Warwick Agreement on femoroacetabular impingement syndrome (FAI syndrome): an international consensus statement', *British Journal of Sports Medicine*, 50(19), pp. 1169–1176. doi: 10.1136/bjsports-2016-096743.

Griffiths, D. J. (1999) *Introduction to Electrodynamics*. Third. Prentice Hall.

Hamdi, M. and Awad, M. (2014) 'Lower limb motion tracking using IMU sensor network Lower Limb Motion Tracking Using IMU Sensor', (December). doi: 10.1109/CIBEC.2014.7020957.

Hunter, J. D. (2007) 'Matplotlib: A 2D graphics environment', *Computing in Science and Engineering*, 9(3), pp. 99–104. doi: 10.1109/MCSE.2007.55.

'ISB recommendation on joint coordinate' (2002), 35, pp. 543–548.

Jena, E., Peiselt, K. and Gleichmann, N. (2013) 'Unambiguous position and orientation tracking using a rotating magnet', *Journal of Applied Physics*, 114502. doi: 10.1063/1.4821506.

Kadaba, M. P., Ramakrishnan, H. K. and Wootten, M. E. (1990) 'Measurement of Lower Extremity Kinematics During Level Walking', pp. 383–392.

Kortier, H. G. *et al.* (2015) 'Hand Pose Estimation by Fusion of Inertial and Magnetic Sensing Aided by a Permanent Magnet', *IEEE transactions on Neural Systems and Rehabilitation Engineering*, 23(5).

Lambrecht, J. M. and Kirsch, R. F. (2014) 'Miniature Low-Power Inertial Sensors : Promising Technology for Implantable Motion Capture Systems', 22(6), pp. 1138–1147.

Lemaître, G., Nogueira, F. and Aridas, C. K. (2017) 'Imbalanced-learn: A Python Toolbox to Tackle the Curse of Imbalanced Datasets in Machine Learning', *Journal of Machine Learning Research*, 18(17), pp. 1–5. Available at: <http://jmlr.org/papers/v18/16-365.html>.

Lin, Z. *et al.* (2011) 'Development of the Wireless Ultra-Miniaturized Inertial Measurement Unit WB-4: Preliminary Performance Evaluation', pp. 6927–6930.

Llamas, C. *et al.* (2017a) 'Open source hardware based sensor platform suitable for human gait identification', *Pervasive and Mobile Computing*. Elsevier B.V., 38, pp. 154–165. doi: 10.1016/j.pmcj.2016.07.003.

Llamas, C. *et al.* (2017b) 'Open source hardware based sensor platform suitable for human gait identification', *Pervasive and Mobile Computing*. Elsevier B.V., 38, pp. 154–165. doi: 10.1016/j.pmcj.2016.07.003.

López-Nava, I. H. and Muñoz-Meléndez, A. (2016) 'Wearable Inertial Sensors for Human Motion Analysis : A Review', 16(22), pp. 7821–7834.

Mahoney, A. W., Member, S. and Abbott, J. J. (2014) 'Generating Rotating Magnetic Fields With a Single Permanent Magnet for Propulsion of Untethered Magnetic Devices in a Lumen', 30(2), pp. 411–420.

McKinney, W. (2010) 'Data Structures for Statistical Computing in Python', in van der Walt, S. and Millman, J. (eds) *Proceedings of the 9th Python in Science Conference*, pp. 51–56.

'MIT @ opensource.org' (no date). Available at: <https://opensource.org/licenses/MIT>.

- Ng, V. Y. *et al.* (2010) 'Efficacy of Surgery for Femoroacetabular Impingement: A Systematic Review', *The American Journal of Sports Medicine*, 38(11), pp. 2337–2345. doi: 10.1177/0363546510365530.
- Olivares, A. *et al.* (2011) 'Wagyromag : Wireless sensor network for monitoring and processing human body movement in healthcare applications', *Journal of Systems Architecture*. Elsevier B.V., 57(10), pp. 905–915. doi: 10.1016/j.sysarc.2011.04.001.
- Packer, J. D. and Safran, M. R. (2015) 'The etiology of primary femoroacetabular impingement: genetics or acquired deformity?', *Journal of Hip Preservation Surgery*, 2(3), pp. 249–257. doi: 10.1093/jhps/hnv046.
- Parvizi, J., Leunig, M. and Ganz, R. (2007) 'Femoroacetabular Impingement', *J. Am. Acad. Orthop. Surg.*, 15(9), pp. 561–570. doi: 10.1097/01.blo.0000096804.78689.c2.
- Paul, E. and Frederick, J. (2005) 'Three-dimensional computed tomography of the hip in the assessment of femoroacetabular impingement'.
- Pedregosa, F. *et al.* (2011) 'Scikit-learn: Machine Learning in Python', *Journal of Machine Learning Research*, 12, pp. 2825–2830.
- PNI Corporation (2016) 'User manual RM3100'.
- Qingde Li and Griffiths, J. G. (2004) 'Least squares ellipsoid specific fitting', *Geometric Modeling and Processing, 2004. Proceedings, 2004*, pp. 335–340. doi: 10.1109/GMAP.2004.1290055.
- Ramos, H. G. and Ribeiro, A. L. (2014) 'Present and Future Impact of Magnetic Sensors in NDE', *Procedia Engineering*. Elsevier B.V., 86, pp. 406–419. doi: 10.1016/j.proeng.2014.11.054.
- Renaudin, V., Afzal, M. H. and Lachapelle, G. (2010) 'Complete triaxis magnetometer calibration in the magnetic domain', *Journal of Sensors*, 2010. doi: 10.1155/2010/967245.
- Roetenberg, D. *et al.* (2007) 'A portable magnetic position and orientation tracker'. Elsevier B.V., 135(2), pp. 426–432. doi: 10.1016/j.sna.2006.08.020.
- Röling, M. A. *et al.* (2015) 'A quantitative non-invasive assessment of femoroacetabular impingement with CT-based dynamic simulation - cadaveric validation study', *BMC Musculoskeletal Disorders*, 16(1), p. 50. doi: 10.1186/s12891-015-0504-7.
- Ruffaldi, E. *et al.* (2014) 'A novel approach to motion tracking with wearable

sensors based on Probabilistic Graphical Models', in *Proceedings - IEEE International Conference on Robotics and Automation*. IEEE. doi: 10.1109/ICRA.2014.6907013.

Schott, C., Racz, R. and Ag, S. (no date) '54 . 6 : A NEW TWO-AXIS MAGNETIC POSITION SENSOR', pp. 1–5.

Seel, T., Raisch, J. and Schauer, T. (2014) 'IMU-Based Joint Angle Measurement for Gait Analysis', pp. 6891–6909. doi: 10.3390/s140406891.

Siebenrock, K. A. *et al.* (2009) 'Impingement-free Hip Motion', pp. 699–703. doi: 10.1007/s11999-008-0616-6.

Teslabs Engineering - A way to calibrate a magnetometer (no date). Available at: <https://teslabs.com/articles/magnetometer-calibration/> (Accessed: 20 August 2018).

Volpon, J. B. (2016) *Femoroacetabular impingement, Revista Brasileira de Ortopedia (English Edition)*. doi: 10.1016/j.rboe.2016.10.006.

'www.adafruit.com' (no date). Available at: <https://www.adafruit.com/>.

'www.sparkfun.com' (no date). Available at: <https://www.sparkfun.com/>.

Appendix A: Ethical approval

Approved with Stipulations

New Application

28/05/2018

Project ID: 1999

HREC Reference #: S18/04/077

Title: Hip motion tracking pilot study

Dear Mr Philip Van Niekerk,

The Response to Modifications received on 21/05/2018 14:56 was reviewed by members of the Health Research Ethics Committee 2 (HREC2) via Minimal Risk Review procedures on 28/05/2018 and was approved with stipulations.

Please note the following information about your approved research protocol:

Protocol Approval Period: 28-May-2018 – 27-May 2019.

The stipulations of your ethics approval are as follows:

1. Thank you for your clear and comprehensive response to the points raised. The study is now approved, however, you are requested to please correct the following typos in the informed consent form:
 - There is no individual benefit, but the device will hopefully be used to study hip impingement syndrome and help **asses** those
 - There are no foreseeable risks in **talking** part in this study.
 - There is no foreseeable **risks** (change to "risk") of injury associated with the study.

Please remember to use your Project ID [1999] and ethics reference number on any documents or correspondence with the HREC concerning your research protocol.

Please note that this decision will be ratified at the next HREC full committee meeting. HREC reserves the right to suspend approval and to request changes or clarifications from applicants. The coordinator will notify the applicant (and if applicable, the supervisor) of the changes or suspension within 1 day of receiving the notice of suspension from HREC. HREC has the prerogative and authority to ask further questions, seek additional information, require further modifications, or monitor the conduct of your research and the consent process.

After Ethical Review:

Please note you can submit your progress report through the online ethics application process, available at: <https://apply.ethics.sun.ac.za> and the application should be submitted to the Committee before the year has expired. Please see [Forms and Instructions](#) on our HREC website for guidance on how to submit a progress report.

The Committee will then consider the continuation of the project for a further year (if necessary). Annually a number of projects may be selected randomly for an external audit.

Provincial and City of Cape Town Approval

Please note that for research at a primary or secondary healthcare facility, permission must still be obtained from the relevant authorities (Western Cape Department of Health and/or City Health) to conduct the research as stated in the protocol. Please consult the Western Cape Government website for access to the online Health Research Approval Process, see: <https://www.westerncape.gov.za/general-publication/health-research-approval-process>. Research that will be conducted at any tertiary academic institution requires approval from the relevant hospital manager. Ethics approval is required BEFORE approval can be obtained from these health authorities.

We wish you the best as you conduct your research.

For standard HREC forms and instructions, please visit: [Forms and Instructions](#) on our HREC website (www.sun.ac.za/healthresearchethics)

If you have any questions or need further assistance, please contact the HREC office at 021 938 9677.

Yours sincerely,

Francis Masiye

HREC Coordinator,

Health Research Ethics Committee 2 (HREC2).

National Health Research Ethics Council (NHREC) Registration Number:

REC-130408-012 (HREC1)-REC-230208-010 (HREC2)

Federal Wide Assurance Number: 00001372

Office of Human Research Protections (OHRP) Institutional Review Board (IRB) Number:
IRB0005240 (HREC1)-IRB0005239 (HREC2)

The Health Research Ethics Committee (HREC) complies with the SA National Health Act No. 61 of 2003 as it pertains to health research. The HREC abides by the ethical norms and principles for research, established by the [World Medical Association \(2013\) Declaration of Helsinki](#); [Ethical Principles for Medical Research Involving Human Subjects](#); the South African Department of Health (2006). [Guidelines for Good Practice in the Conduct of Clinical Trials with Human Participants in South Africa \(2nd edition\)](#); as well as the Department of Health (2015). Ethics in Health Research: Principles, Processes and Structures (2nd edition).

The Health Research Ethics Committee reviews research involving human subjects conducted or supported by the Department of Health and Human Services, or other federal departments or agencies that apply the Federal Policy for the Protection of Human Subjects to such research (United States Code of Federal Regulations Title 45 Part 46); and/or clinical investigations regulated by the Food and Drug Administration (FDA) of the Department of Health and Human Services.

Appendix B: Results

B.1 Sample results from pilot study 2

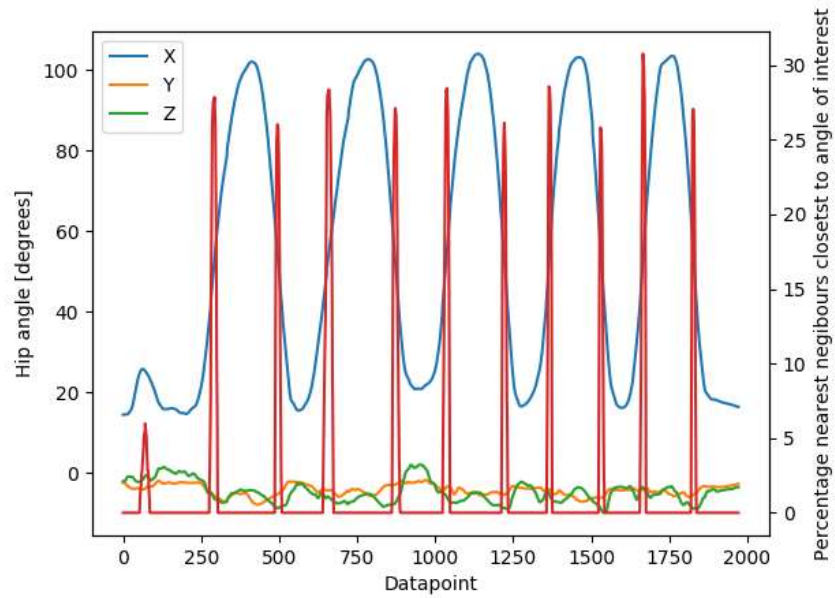


Figure 35: Percentage nearest neighbours closest to the point of interest and hip angle for 5 squats

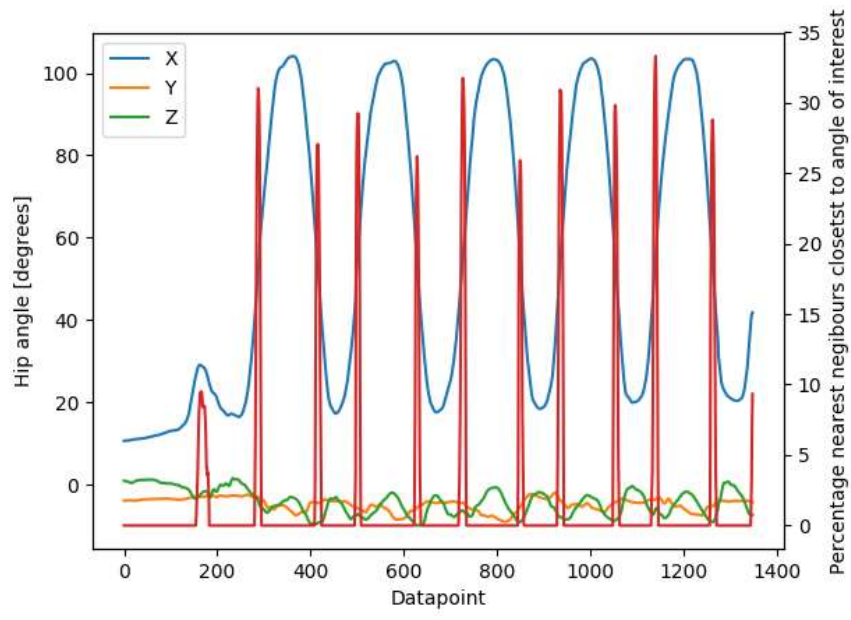


Figure 36: Percentage nearest neighbours closest to the point of interest and hip angle for 5 squats

B.2 Sample hip motion data from Vicon

Below sample outputs from the Vicon are plotted to display the low range of hip angles in the Y and Z direction

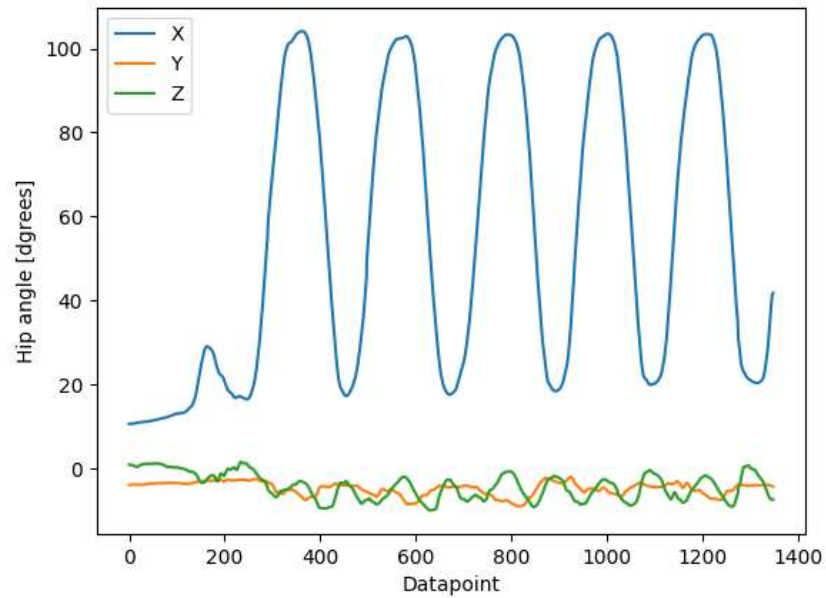


Figure 37: Hip angle data from Vicon for squat movement

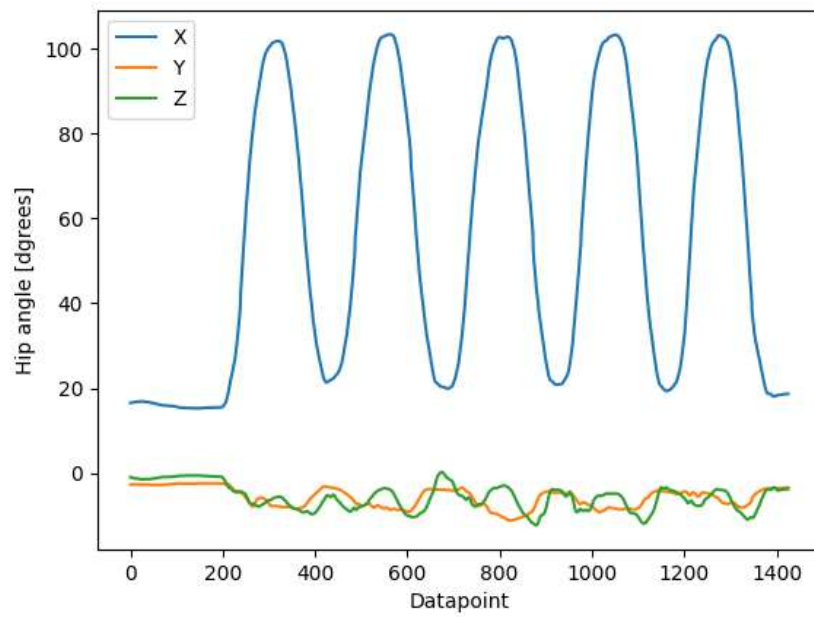


Figure 38: Hip angle data from Vicon for lunge movement

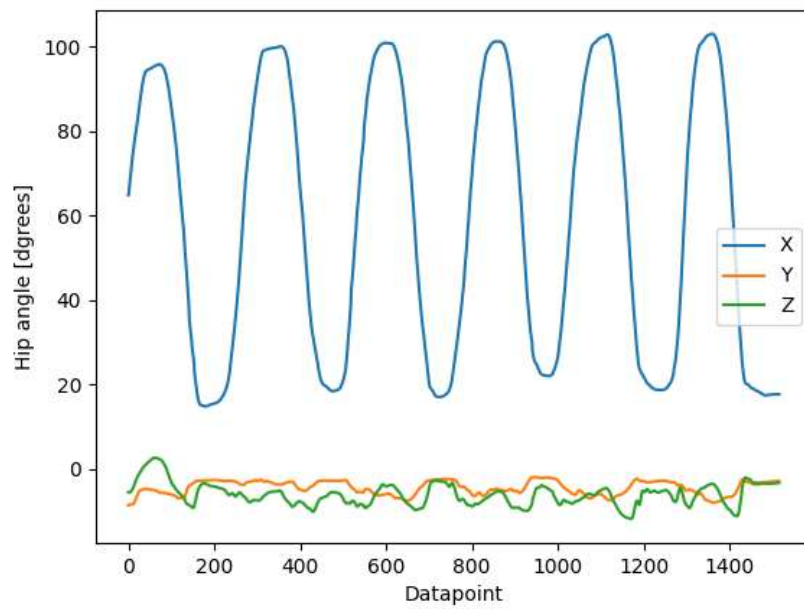


Figure 39: Hip angle data from Vicon for squat movement

Appendix C: Normal hip range of motion

MOVEMENT	THE NORMAL RANGE OF MOTION (DEGREES)
FLEXION (FL)	120
ABDUCTION (ABD)	50
INTERNAL ROTATION (IN)	50
IN WITH 50 ABD	40
EXTERNAL ROTATION (EX) WITH 30 ABD	40
IN WITH 50 FL	30
IN WITH 30 FL, 20 ADDUCTION (AD)	50
IN WITH 60 FL, 20 AD	40
IN WITH 90 FL, 30 AD	30
EXT WITH 15 EXL	15

Appendix D: Review of studies

REVIEW OF STUDIES RELATED TO IMU

PAPERS	Self-developed / commercial hardware	Sensor fusion	Accuracy	Additional comments	Reference
XSENS MVN: CONSISTENT TRACKING OF HUMAN MOTION USING INERTIAL SENSING	Commercial	Commercial	10.1 degrees hip max RMS error when compared to OpenSim simulation 4.8 degrees RMS error for static pose compared to Vicon	The authors state system is accurate through 90 min test.	(Chepers, Giuberti and Bellusci, 2018)
DEVELOPMENT OF THE WIRELESS ULTRA-MINIATURIZED INERTIAL MEASUREMENT UNIT WB-4: PRELIMINARY PERFORMANCE EVALUATION	Self-developed	Self-developed in Matlab	Max RMS error in yaw angle: 5.46 degrees	Tested on a rig and not on a person. Validated against a Vicon	(Lin <i>et al.</i> , 2011)

WAGYROMAG: WIRELESS SENSOR NETWORK FOR MONITORING AND PROCESSING HUMAN BODY MOVEMENT IN HEALTHCARE APPLICATIONS	Self-developed	Self-developed using Kalman filter	No- validation is done	Detailed description of sensor fusion algorithms	(Olivares <i>et al.</i> , 2011)
OPEN SOURCE HARDWARE BASED SENSOR PLATFORM SUITABLE FOR HUMAN GAIT IDENTIFICATION:	Self-developed	Self-developed using extended Kalman filter	No- validation is done	Open source development of hardware signal processing	(Llamas <i>et al.</i> , 2017)
LOWER LIMB MOTION TRACKING USING IMU SENSOR NETWORK	Self-developed	Self-developed using Kalman filter	Max error of 13.3 degrees in hip joint	The large error in one gait cycle. Lower limb-specific	(Hamdi and Awad, 2014)
JOINT ANGLE TRACKING WITH INERTIAL SENSORS	commercial	Self-developed using unscented Kalman filter	The average error of 2.1 degrees on robotic arm	Validated on robotic arm over a short period of time (30 s)	(El-gohary, 2013)
DEVELOPMENT OF WEARABLE INERTIAL SENSORS FOR	commercial	commercial	Not applicable	Large units	(Chan and Ripin, 2013)

MEASUREMENT OF HAND ARM TREMORS					
IMU-BASED JOINT ANGLE MEASUREMENT FOR GAIT ANALYSIS	commercial (Xsens)	commercial	RMS error on knee joint 3.3 degrees	Short experiment duration	(Seel, Raisch and Schauer, 2014)
WEARABLE INERTIAL SENSORS FOR HUMAN MOTION ANALYSIS REVIEW	commercial and self-developed			Review of multiple IMU base studies.	(López-Nava and Muñoz-Meléndez, 2016)
REAL-TIME HUMAN MOTION CAPTURE DRIVEN BY A WIRELESS SENSOR NETWORK	self-developed			Focus on speed of real-time algorithms	(Chen <i>et al.</i> , 2015)
A NOVEL APPROACH TO MOTION TRACKING WITH WEARABLE SENSORS BASED ON PROBABILISTIC GRAPHICAL MODELS				Overview of different filters and the advantages of each	(Ruffaldi <i>et al.</i> , 2014)
A NOVEL COMPLIMENTARY FILTER FOR TRACKING HIP ANGLES DURING CYCLING USING WIRELESS INERTIAL SENSORS AND DYNAMIC ACCELERATION ESTIMATION	Commercial (Xsens)	Self-developed algorithms	6.7 degree mean error in frontal plane in best results but differ greatly due to calibration	Specific to hip motion tracking. Calibration error explained	(Cockcroft, Muller and Scheffer, 2014)

REVIEW OF STUDIES RELATED TO MAGNETIC FIELD TRACKING

PAPER	Notes	Reference
MAGNID: TRACKING MULTIPLE MAGNETIC TOKENS	Rotating, small permanent magnets. Machine learning algorithm used to calibrate magnet positions	(Bianchi and Oakley, 2015)
A NEW TWO-AXIS MAGNETIC POSITION SENSOR	Magnetic field modeling used to determine location of magnet	(Schott, Racz and Ag, no date)
A PORTABLE MAGNETIC POSITION AND ORIENTATION TRACKER	3 axis rotating source electromagnet, magnetometers on limbs Magnetic field model through dipole model	(Roetenberg <i>et al.</i> , 2007)
UTRACK: 3D INPUT USING TWO MAGNETIC SENSORS	Single permanent magnet tracking over a short distance with magnetic field modeling	(Chen <i>et al.</i> , 2013)
HAND POSE ESTIMATION BY FUSION OF INERTIAL AND MAGNETIC SENSING AIDED BY A PERMANENT MAGNET	Tracking of a single magnet on hand from trunk A lot of recommendations 2 magnetometer and a permanent magnet	(Kortier <i>et al.</i> , 2015)

	Large system	
UNAMBIGUOUS POSITION AND ORIENTATION TRACKING USING A ROTATING MAGNET	Large rotating magnet tracked in 3d space with 1% error over 17m. Ellipse magnetic field model used.	(Jena, Peiselt and Gleichmann, 2013)
A NEW METHOD FOR MAGNETIC POSITION AND ORIENTATION TRACKING	Generating elliptic magnetic field with rotation permeant magnet	(Seel, Raisch and Schauer, 2014)
GENERATING ROTATING MAGNETIC FIELDS WITH A SINGLE	Magnetic field dipole model explained	(Mahoney, Member and Abbott, 2014)